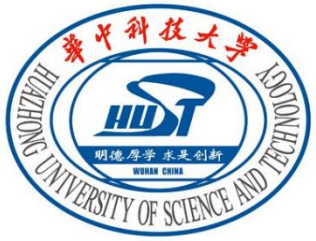

科技论文写作

（一）定义、分类与结构

人工智能与自动化学院

谭 山

shantan@hust.edu.cn

2024年6月11日

科学研究有三个阶段，首先是开拓，其次是完成，第三是发表。

——法拉第

科技论文的重要性

- 英国文学家萧伯纳：倘若你有一个苹果，我也有一个苹果，我们彼此交换，你和我仍各有一个苹果。但倘若你有一种思想，我也有一种思想，我们彼此交流，那我们将各有两种思想。
- 卢嘉锡：一个只会创作，不会表达的人，不算一个真正的科技工作者。

◆ 交流 ：撰写论文主要是与同行交流，既是介绍作者的工作促进科学技术进步，也是**吸收别人意见**改进作者工作的重要步骤。

◆ 提高 ：撰写论文是**对研究工作的整理、总结和精练的过程**，**有助于发现研究中的空白点和薄弱环节**，产生新的想法，进一步提高研究质量。

◆ 训练：科技写作是科技工作者必要的基本训练。 熟练掌握Word, EndNote, Latex等。

科技论文

- 必须完整回答为什么研究（why），怎么样研究（how）和结果是什么（what）。
- 论文强调科学性、创造性、逻辑性和有效性。

科技论文基本特点

- ◆科学性
- ◆学术性
- ◆首创性
- ◆理论性
- ◆规范性
- ◆有效性

科技论文特点：科学性

科学性是科技论文的生命。

- **内容的科学性**：论点和结论必须真实、科学。要求作者必须具有严谨的治学作风和实事求是的科学态度。
- **论据和论证必须科学**。论据真实、典型，真正成为论文的支柱。
- **表述的科学性**：论述表达准确、科学。脉络清晰、措辞严谨、概念准确、条理清楚、结构完整。
- **技术和方法可重复性高**，写作是要详细介绍必要的、关键的内容。
- 结果的**可比性和逻辑性**。设立对比观察，并用统计学的方法处理观察结果。

表述不严谨的例子

A radiologist manually adjusted tumor segmentation results, when necessary, by visually inspecting the associated contours and the fused PET/CT images.

Reviewer: This sentence sounds a little iffy. I would recommend specifying what "when necessary" means in order to make the sentence sound a little more scientific.

修改：

A radiologist checked all tumor segmentation results by visually inspecting the associated contours and the fused PET/CT images. No obvious segmentation error was observed except for one tumor that showed three adjacent regions barely disconnected. The radiologist manually connected the three regions into a single ROI.

表达不严谨的例子：

The proposed model can reduce the influence of these uncertainties on the accuracy of the model to some extent.

表达较严谨的例子：

Particularly, on seven financial market indices, the proposed model with the direction regularization term achieves the highest POCID (32.04% higher than that of CNN) and the lowest MAPE (37.36% lower than that of DA-RNN).

科技论文特点：学术性

新：论点或方法上具有创新；

深：研究有深度，能抓住问题本质；

实：材料具有权威性。

科技论文特点: 首创性

首创性——科技论文的灵魂

- 创造是科学的本质
- 论文中揭示的事物现象的本质、规律和特性，应该是前人未见的或部分未见的。
- 文章要有所发现，有所发明，有所创造。
- 不是对前人工作的复述、模仿或者解释。

科技论文特点: 理论性

- 学术论文不能停留于事实、现象的罗列，必须探究事物的本质及规律。
- 写论文必须运用理论思维、通过对事实的抽象、概括、说理、辨析和严密的逻辑论证，将一般现象上升到一定的理论高度。

科技论文特点：规范性

规范性是指对论文语言文字和表达形式等方面的质量要求。

- 科技报告、学位论文等编写格式国家制定了统一的标准；
- 国际科技行业协会、组织、出版社等对论文格式有严格规定，包括排版、图表制作、公式编辑、符号使用、参考文献格式等等。

科技论文的特点：有效性

- 经过相关专业**同行审阅(Peer Review)**、在正式的科技刊物上反表的科技论文才被承认位完备和有效的。
- 正式刊物发表的论文、发明专利论文，都会成为人类知识宝库中的一个组成部分。

科技论文分类

按照 **论文的作用** 分：**学术论文、技术论文、学位论文**等。

- **学术论文**：

学术性期刊或学术会议发表的论文，以报道学术研究成果为主要内容。反映该学科领域最新、最前沿的科学水平和发展动向。

- **学位论文**：学位申请者提交的论文

学士论文：反映作者具有专门的知识和技能，具有从事科学技术研究或者担负专门技术工作的初步能力。

硕士论文：具有一定创新，掌握专业基础知识及科学研究方法，具备一定的科研能力。

博士论文：反映出作者具有坚实广博的基础理论知识和系统、深入的专门知识，具有独立从事科学技术研究工作的能力，应反映出该科学技术领域最前沿的独创性成果。

学术论文结构

标题 Title	作者署名和地址 Authors	摘要 Abstract	关键词 Key words
引言 Introduction	方法 Method	实验结果 Results	讨论 Discussion
结论 Conclusions	致谢 Acknowledgements	参考文献 References	附录 Appendix
注释 Notes			

例1： 孙涛论文

论文撰写

写作时，回答好下列问题

1. 研究动机何在？
2. 前人已经做了什么？存在哪些问题？
3. 自己的实质进展
4. 研究问题的提法
5. 理论分析，数值模块和实验研究基本过程
6. 如何令人信服地演绎和分析成果？
7. 从哪些角度验证成果正确性和有效性？
8. 结论是什么
9. 进一步研究的问题

- 科技论文必须完整回答：
  - 为什么研究 (**why**)
  - 怎么样研究 (**how**)
  - 结果是什么 (**what**)

学术论文结构

题目：充分概括论文内容和主题

摘要：概述主题、方法和主要成果

引言：叙述论文写作动机，点明立题背景，概述前人相关成果及论文

正文：所研究的具体问题，研究途径(理论分析，数值模拟，实验方法)，研究步骤，主要成果的详尽分析

结论：概述主要研究结论和前景展望

致谢：感谢资助方和曾给予重要帮助的人员

参考文献：相关经典和近代文献

附录：不宜列入正文的演绎过程和某些依据，如程序数据等。

学术论文结构：例子

Are All Apples Red?

by

Ida Cortland

Abstract:

We examined several apples' color. Although most are red, some are not.

Introduction:

An age-old question is: are all apples red? MacIntosh (1993) thought so. G. Smith (1999) begs to differ. We hope to resolve this issue once and for all.

Methods:

We went to the local grocery store and bought one of every apple they had. We took them home and looked at them.

Results:

We found four red apples, one green apple, and two yellow apples.

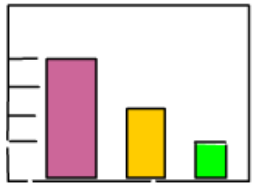

Figure 1

Discussion:

Since we found one yellow apple and two green apples, it must be true that all apples are not red. We concur with G. Smith's findings.

References:

MacIntosh (1993) *Journal of Fruit Science*. 4(3): 121-135.

Smith, G. (1999) *Apple Technology Today.* 7(3):4-8.

学术论文结构

摘要

- (1). We proposed a method **D** to solve **problem X**. (2). This method outperforms methods A, B, and C.

前言

- (1). Problem X is important; (2). Previous works A, B, and C have been done; (3). A, B, and C have their weakness; (4). We proposed method **D** without the weakness.

正文

- Your work **D** (Theoretic analysis of **D**)

实验

- Comparison (**D** against A, B, and C for problem X)

讨论

- (1). Why **D** is better; (2). Strength and weakness of **D**; (3). Future works on **D**

结论

- Our method **D** works well.

题目

Title, 标题，题目，文题，题名，篇名

- 论文的高度概括，一般不超过20个字，不能过短以致太笼统
- 研究人员常常通过快速浏览论文题目，判别：
  - ✓ 论文是否与自己的研究相关
  - ✓ 是否进一步阅读该论文

有时希望：引人入胜，吸引读者的注意力；
看到题目，读者有继续深入阅读的冲动

基本要求：

阐述具体、用语简洁

文题相称，确切鲜明

重点突出，主题明确

反映论点，概括全文

题目

题目种类

- 名词性题目：最常见
- 复合标题：带冒号(英文)或破折号(中文)的标题
- 完整句子

题目中可包含逗号、括号，引号和破折号等，但一般不使用分号（；）和斜杠（/）。

长标题并不总是不好：

- 更长的标题可包含更多关键词，搜索引擎更易发现
- 研究表明标题的长度与引文数量成正相关
- 复合标题的可发现性有增加趋势

题目

名词短语，由一个或几个名词加上前、后置定语构成 (最常见)

[1] T. Sun, N. Sun, J. Wang, and S. Tan, "Iterative CBCT reconstruction using Hessian penalty," Physics in medicine and biology, vol. 60, pp. 1965-1987, Feb 12 2015.

[2] Y. LeCun, Y. Bengio, and G. Hinton, "Deep learning," Nature, vol. 521, pp. 436-444, 2015

复合题目

[3] B. Hitaj, G. Ateniese, and F. Perez-Cruz, "Deep models under the GAN: information leakage from collaborative deep learning," in Proceedings of the 2017 ACM SIGSAC Conference on Computer and Communications Security, 2017, pp. 603-618.

句子作为题目 (容易引起读者关注)

[4] D. Castelvecchi, "Can we open the black box of AI?," Nature News, vol. 538, p. 20, 2016.

[5] P. Chatterjee and P. Milanfar, "Is denoising dead?," IEEE Transactions on Image Processing, vol. 19, pp. 895-911, 2009.

[6] A. Vaswani, N. Shazeer, N. Parmar, J. Uszkoreit, L. Jones, A. N. Gomez, et al., "Attention is all you need," in Advances in neural information processing systems, 2017, pp. 5998-6008.

- 篇名简短，不超过20个字。

➢ 尽可能删去多余词组。

《XX港自引船增多对安全的影响及对策研究》

《XX港自引船增多对安全的影响及对策》

➢ 避免将同义词或近义词连用

《叶轮式增氧机叶轮受力分析探讨》

《叶轮式增氧机叶轮受力分析》

- 题名结构合理，符合现代汉语语法、修辞和逻辑规则
- 一般不用动宾结构

《研究一种制取苯已醛的新方法》，可改为：《一种苯已醛制取的新方法的研究》，再按精炼原则，改为：《一种制取苯已醛的新方法》

- 注意选用定语词组的类型

《研究模糊关系数据库的几个基本理论问题》(动宾结构)，可改为《模糊关系数据库研究的几个基本理论问题》，若改为《模糊关系数据库研究中的几个基本理论问题》，表达更清楚。

- 选词要准确：

《煎炸油质量测试仪的研制》，改为：《煎炸油品质测试仪的研制》

- 避免“的”的多用和漏用（联合词组，偏正词组、主谓词组、动宾词组、介词词组做定语时，中心语之前需用“的”）

《专家系统结构的分析》，不如《专家系统结构分析》通顺简练；

《高层建筑变水量供水电气控制系统》，不如《高层建筑变水量供水的电气控制系统》清楚。

署名

- 《中华人民共和国著作权法》：“著作权属于作者”，著作权包括“署名权，即表明作者身份，在作品上署名的权利”
- 署名权表明文责自负的承诺

指论文一经发表，署名者即应对论文负法律责任，负政治上、科学上的责任。如果论文中存在剽窃、抄袭内容，或者存在政治上、科学上或技术上的错误，那么署名者就应完全负责，署名即表示作者愿意承担这些责任。

署名对象

- 署名者只限于那些参与选定研究课题和制定研究方案、直接参加全部或主要部分研究工作并作出主要贡献，以及参加论文撰写并能对内容负责，同时对论文具有答辩能力的人员；
- 仅参加部分工作的合作者、按研究计划分工负责具体小项的工作者、某一项测试任务的承担者，以及受委托进行分析检验和观察的辅助人员等，均不应署名，但署名者可以将他们作为参加工作人员——列入“致谢”段。

署名

- 署名位于标题下方，工作单位署全称；
- 主要作者在前，次要作者在后；
- 物理、数学有时按照姓式字母顺序排名；
- 通信作者：指导论文整个完成过程的人，一般为导师，资历较高。

Email：不用私人邮箱，使用xxx@hust.edu.cn

署名

2588 IEEE TRANSACTIONS ON MEDICAL IMAGING, VOL. 36, NO. 12, DECEMBER 2017

Low-Dose CBCT Reconstruction Using Hessian Schatten Penalties

Liang Liu, Xinxin Li, Kai Xiang, Jing Wang, and Shan Tan, *Member, IEEE*

Abstract— Cone-beam computed tomography (CBCT) has been widely used in radiation therapy. For accurate patient setup and treatment target localization, it is important to obtain high-quality reconstruction images. The total variation (TV) penalty has shown the state-of-the-art performance in suppressing noise and preserving edges for statistical iterative image reconstruction, but it sometimes leads to the so-called staircase effect. In this paper, we proposed to use a new family of penalties—the Hessian Schatten (HS) penalties—for the CBCT reconstruction. Consisting of the second-order derivatives, the HS penalties are able to reflect the smooth intensity transitions of the underlying image without introducing the staircase effect. We discussed and compared the behaviors of several convex HS penalties with orders 1, 2, and + ∞ for CBCT reconstruction. We used the majorization-minimization approach with a primal-dual formulation for the corresponding optimization problem. Experiments on two digital phantoms and two physical phantoms demonstrated the proposed penalty family's outstanding performance over TV in suppressing the staircase effect, and the HS penalty with order 1 had the best performance among the HS penalties tested.

Index Terms— CBCT, image reconstruction, TV, staircase effect, Hessian Schatten penalty.

I. Introduction

Cone-beam computed tomography (CBCT) provides volumetric information for patient setup and target localization during radiation therapy. Repeated CBCT scans during a treatment course expose patients to extra imaging radiation doses [1], [2]. Lowering the mAs (tube current exposure time product) level in CBCT acquisition can reduce the imaging dose and associated risks to patients [3]. However, the quality of the reconstructed low-mAs image can be dramatically degraded due to excessive noise [4], [5].

Statistical iterative reconstruction (SIR) algorithms have been used to improve the quality of low-dose CBCT imaging [6], [7]. Commonly used penalty terms in SIR include the isotropic quadratic penalty [8], the Huber penalty [9], and the total variation (TV) penalty [10]–[12].

Originally introduced for image de-noising by Rudin *et al.* [10], the TV penalty has shown state-of-the-art performance in preserving edges and suppressing noise for CBCT imaging [10]–[24]. Various TV-based CBCT reconstruction algorithms have been studied and evaluated in the last three decades [10]–[24]. Sidky and Pan proposed to minimize the TV penalty subject to a non-negative constraint for sparse-view projection reconstruction, where the TV objective function was minimized by steepest descent with an adaptive step size, and the non-negative constraint was enforced by projection onto convex sets (POCS) [13], [18], [19]. Han *et al.* [20] studied the selection of parameter values in the constrained TV minimization-based reconstruction and showed, with both visualization and quantitative assessments, that the reconstructions were greatly improved, relative to the clinical FDK reconstruction, in terms of the devised utility metrics. Bian *et al.* [21] showed that the TV-based iterative algorithm was more robust to different data conditions, such as number of views and exposure levels, than the FDK algorithm for CBCT reconstruction. Hashemi *et al.* [14] proposed a simultaneous deblurring and iterative reconstruction to explicitly account for image unsharpness caused by different factors in the CBCT reconstruction formulation when using the TV penalty. Huang and Hsiao [15] proposed an iterative reconstruction method to accelerate the ordered-subsets reconstruction with a power factor, in combination with the TV minimization method.

The major limitation of the TV penalty is that it sometimes causes the staircase effect in reconstructed images [25], [26], particularly a… first-order derivatives, *i.e.*, minimizing the intensity difference between neighboring pixels. Therefore, it tends to produce piecewise constant reconstructed images, even when the underlying images are not necessarily piecewise constant.

To avoid the staircase effect due to the TV penalty, Yan *et al.* [26] considered the anisotropic edge property

Manuscript received August 7, 2017; revised September 22, 2017; accepted October 15, 2017. Date of publication October 24, 2017; date of current version November 29, 2017. This work was supported by the National Natural Science Foundation of China under Grant 61375018 and Grant 61672253. The work of J. Wang was supported in part by the Cancer Prevention and Research Institute of Texas under Grant RP130109 and Grant RP110562-P2, in part by the National Institute of Biomedical Imaging and Bioengineering under Grant R01 EB020366, and in part by the American Cancer Society under Grant RSG-13-326-01-CCE. *(Corresponding authors: Jing Wang; Shan Tan.)*

L. Liu, X. Li, K. Xiang, and S. Tan are with the Key Laboratory of Image Processing and Intelligent Control of Ministry of Education of China, and the School of Automation, Huazhong University of Science and Technology, Wuhan, Hubei 430074, China (e-mail: liangliu@hust.edu.cn; xxl117@hust.edu.cn; u201314635@hust.edu.cn; shantan@hust.edu.cn).

J. Wang is with the Department of Radiation Oncology, University of Texas Southwestern Medical Center, Dallas, TX 75390 USA (e-mail: jing.wang@utsouthwestern.edu).

Color versions of one or more of the figures in this paper are available online at http://ieeexplore.ieee.org.

Digital Object Identifier 10.1109/TMI.2017.2766185

Low-Dose CBCT Reconstruction Using Hessian Schatten Penalties

Liang Liu, Xinxin Li, Kai Xiang, Jing Wang, and Shan Tan, *Member, IEEE*

L. Liu, X. Li, K. Xiang, and S. Tan are with the Key Laboratory of Image Processing and Intelligent Control of Ministry of Education of China, and the School of Automation, Huazhong University of Science and Technology, Wuhan, Hubei 430074, China (e-mail: liangliu@hust.edu.cn; xxl117@hust.edu.cn; u201314635@hust.edu.cn; shantan@hust.edu.cn).

J. Wang is with the Department of Radiation Oncology, University of Texas Southwestern Medical Center, Dallas, TX 75390 USA (e-mail: jing.wang@utsouthwestern.edu).

署名

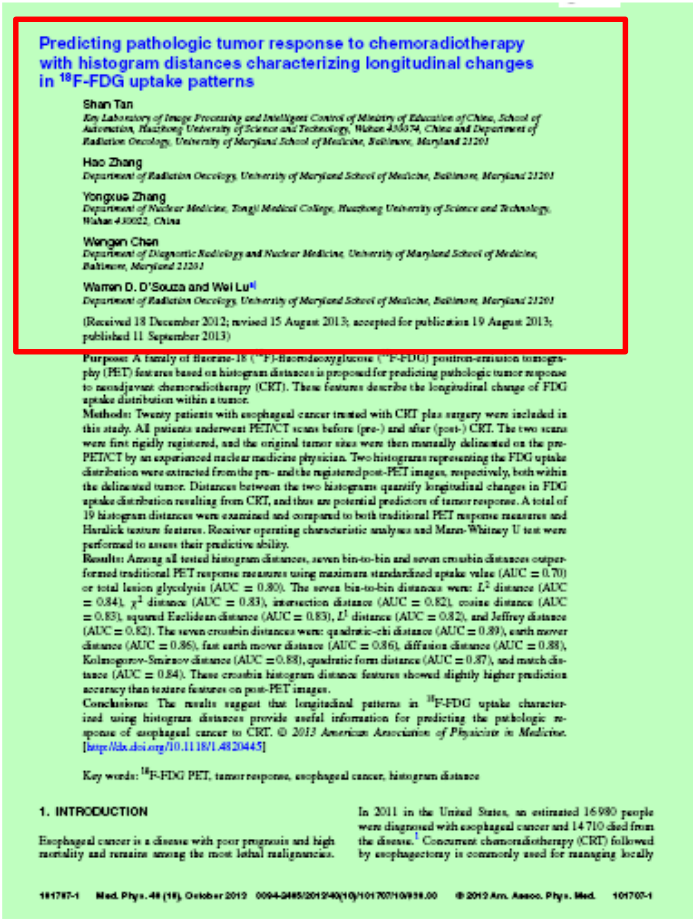

Predicting pathologic tumor response to chemoradiotherapy with histogram distances characterizing longitudinal changes in ^{18}F-FDG uptake patterns

Shan Tan
Key Laboratory of Image Processing and Intelligent Control of Ministry of Education of China, School of Automation, Huazhong University of Science and Technology, Wuhan 430074, China and Department of Radiation Oncology, University of Maryland School of Medicine, Baltimore, Maryland 21201

Hao Zhang
Department of Radiation Oncology, University of Maryland School of Medicine, Baltimore, Maryland 21201

Yongxue Zhang
Department of Nuclear Medicine, Tongji Medical College, Huazhong University of Science and Technology, Wuhan 430022, China

Wengen Chen
Department of Diagnostic Radiology and Nuclear Medicine, University of Maryland School of Medicine, Baltimore, Maryland 21201

Warren D. D'Souza and Wei Lu[a)]
Department of Radiation Oncology, University of Maryland School of Medicine, Baltimore, Maryland 21201

(Received 18 December 2012; revised 15 August 2013; accepted for publication 19 August 2013; published 11 September 2013)

Purpose: A family of fluorine-18 (^{18}F)-fluorodeoxyglucose (^{18}F-FDG) positron-emission tomography (PET) features based on histogram distances is proposed for predicting pathologic tumor response to neoadjuvant chemoradiotherapy (CRT). These features describe the longitudinal change of FDG uptake distribution within a tumor.
Methods: Twenty patients with esophageal cancer treated with CRT plus surgery were included in this study. All patients underwent PET/CT scans before (pre-) and after (post-) CRT. The two scans were first rigidly registered, and the original tumor sites were then manually delineated on the pre-PET/CT by an experienced nuclear medicine physician. Two histograms representing the FDG uptake distribution were extracted from the pre- and the registered post-PET images, respectively, both within the delineated tumor. Distances between the two histograms quantify longitudinal changes in FDG uptake distribution resulting from CRT, and thus are potential predictors of tumor response. A total of 19 histogram distances were examined and compared to both traditional PET response measures and Haralick texture features. Receiver operating characteristic analyses and Mann–Whitney U test were performed to assess their predictive ability.
Results: Among all tested histogram distances, seven bin-to-bin and seven cross-bin distances outperformed traditional PET response measures using maximum standardized uptake value (AUC = 0.70) or total lesion glycolysis (AUC = 0.80). The seven bin-to-bin distances were: L^2 distance (AUC = 0.84), χ^2 distance (AUC = 0.83), intersection distance (AUC = 0.82), cosine distance (AUC = 0.83), squared Euclidean distance (AUC = 0.83), L^1 distance (AUC = 0.82), and Jeffrey distance (AUC = 0.82). The seven cross-bin distances were: quadratic-chi distance (AUC = 0.89), earth mover distance (AUC = 0.86), fast earth mover distance (AUC = 0.86), diffusion distance (AUC = 0.88), Kolmogorov–Smirnov distance (AUC = 0.88), quadratic form distance (AUC = 0.87), and match distance (AUC = 0.84). These cross-bin histogram distance features showed slightly higher prediction accuracy than texture features on post-PET images.
Conclusions: The results suggest that longitudinal patterns in ^{18}F-FDG uptake characterized using histogram distances provide useful information for predicting the pathologic response of esophageal cancer to CRT. © *2013 American Association of Physicists in Medicine.*
[http://dx.doi.org/10.1118/1.4820445]

Key words: ^{18}F-FDG PET, tumor response, esophageal cancer, histogram distance

1. INTRODUCTION

Esophageal cancer is a disease with poor prognosis and high mortality and remains among the most lethal malignancies. In 2011 in the United States, an estimated 16 980 people were diagnosed with esophageal cancer and 14 710 died from the disease.[1] Concurrent chemoradiotherapy (CRT) followed by esophagectomy is commonly used for managing locally

Predicting pathologic tumor response to chemoradiotherapy with histogram distances characterizing longitudinal changes in ^{18}F-FDG uptake patterns

Shan Tan
Key Laboratory of Image Processing and Intelligent Control of Ministry of Education of China, School of Automation, Huazhong University of Science and Technology, Wuhan 430074, China and Department of Radiation Oncology, University of Maryland School of Medicine, Baltimore, Maryland 21201

Hao Zhang
Department of Radiation Oncology, University of Maryland School of Medicine, Baltimore, Maryland 21201

Yongxue Zhang
Department of Nuclear Medicine, Tongji Medical College, Huazhong University of Science and Technology, Wuhan 430022, China

Wengen Chen
Department of Diagnostic Radiology and Nuclear Medicine, University of Maryland School of Medicine, Baltimore, Maryland 21201

Warren D. D'Souza and Wei Lu[a)]
Department of Radiation Oncology, University of Maryland School of Medicine, Baltimore, Maryland 21201

(Received 18 December 2012; revised 15 August 2013; accepted for publication 19 August 2013; published 11 September 2013)

S. Tan, Howard Zhang, Yongxue Zhang, Wengen Chen, Warren D. D'Souza, and W. Lu, "Predicting Pathologic Tumor Response to Chemoradiotherapy with Histogram Distances Characterizing Longitudinal Changes in 18F-FDG Uptake Patterns," Medical Physics, vol. 40, Oct. 2013.

署名

IOP Publishing | Institute of Physics and Engineering in Medicine Physics in Medicine & Biology
Phys. Med. Biol. 60 (2015) 1965–1987 doi:10.1088/0031-9155/60/5/1965

Iterative CBCT reconstruction using Hessian penalty

Tao Sun[1], Nanbo Sun[1], Jing Wang[2] and Shan Tan[1]

[1] Key Laboratory of Image Processing and Intelligent Control of Ministry of Education of China, School of Automation, Huazhong University of Science and Technology, Wuhan 430074, People's Republic of China
[2] Department of Radiation Oncology, The University of Texas Southwestern Medical Center at Dallas, Dallas, TX 75390, USA

E-mail: shantan@mail.hust.edu.cn and Jing.Wang@UTSouthwestern.edu

Received 13 July 2014, revised 12 November 2014
Accepted for publication 3 December 2014
Published 12 February 2015

Abstract

Statistical iterative reconstruction algorithms have shown potential to improve cone-beam CT (CBCT) image quality. Most iterative reconstruction algorithms utilize prior knowledge as a penalty term in the objective function. The penalty term greatly affects the performance of a reconstruction algorithm. The total variation (TV) penalty has demonstrated great ability in suppressing noise and improving image quality. However, calculated from the first-order derivatives, the TV penalty leads to the well-known staircase effect, which sometimes makes the reconstructed images oversharpen and unnatural. In this study, we proposed to use a second-order derivative penalty that involves the Frobenius norm of the Hessian matrix of an image for CBCT reconstruction. The second-order penalty retains some of the most favorable properties of the TV penalty like convexity, homogeneity, and rotation and translation invariance, and has a better ability in preserving the structures of gradual transition in the reconstructed images. An effective algorithm was developed to minimize the objective function with the majorization-minimization (MM) approach. The experiments on a digital phantom and two physical phantoms demonstrated the priority of the proposed penalty, particularly in suppressing the staircase effect of the TV penalty.

Keywords: cone-beam CT, iterative reconstruction, Hessian regularization, total variation penalty, majorization–minimization approach

(Some figures may appear in colour only in the online journal)

Iterative CBCT reconstruction using Hessian penalty

Tao Sun[1], Nanbo Sun[1], Jing Wang[2] and Shan Tan[1]

[1] Key Laboratory of Image Processing and Intelligent Control of Ministry of Education of China, School of Automation, Huazhong University of Science and Technology, Wuhan 430074, People's Republic of China
[2] Department of Radiation Oncology, The University of Texas Southwestern Medical Center at Dallas, Dallas, TX 75390, USA

E-mail: shantan@mail.hust.edu.cn and Jing.Wang@UTSouthwestern.edu

Received 13 July 2014, revised 12 November 2014
Accepted for publication 3 December 2014
Published 12 February 2015

摘要

- **文摘或提要，提供文献内容梗概。**

- 结构性摘要
  - 目的(Purpose)
  - 方法(Methods)
  - 结果(Results)
  - 结论(Conclusions)
- 非结构性摘要

内容：

- 研究目的和重要性
- 研究完成了哪些工作
- 基本结论、成果，新认识、新见解等。

摘要撰写

摘要中包含的内容(每部分内容一般使用1-2个或几个句子)：

1. **研究了什么问题，为什么重要？**用一个或几个句子，描述研究背景，研究动机和/或要解决的特定问题或假设等；

2. **使用什么方法研究问题？**概述所用方法 （例如，实验方法，模拟方法，理论方法，这些方法的组合等）；

3. **主要发现是什么？**重点描述主要发现，但不超过两点或三点。

4. **得出了什么结论以及更广泛的含义？**这些发现有什么创新？这些发现如何影响研究领域？

结构性摘要

注意方法部分只写方法；结果部分只写结果；生物、医学类科研人员比工科更强调论文结构分离

Purpose: To extract and study comprehensive spatial-temporal ^{18}F-labeled fluorodeoxyglucose ([^{18}F]FDG) positron emission tomography (PET) features for the prediction of pathologic tumor response to neoadjuvant chemoradiation therapy (CRT) in esophageal cancer.

Methods and Materials: Twenty patients with esophageal cancer were treated with trimodal therapy (CRT plus surgery) and underwent [^{18}F]FDG-PET/CT scans both before (pre-CRT) and after (post-CRT) CRT. The 2 scans were rigidly registered. A tumor volume was semiautomatically delineated using a threshold standardized uptake value (SUV) of $\geq$2.5, followed by manual editing. Comprehensive features were extracted to characterize SUV intensity distribution, spatial patterns (texture), tumor geometry, and associated changes resulting from CRT. The usefulness of each feature in predicting pathologic tumor response to CRT was evaluated using the area under the receiver operating characteristic curve (AUC) value.

Results: The best traditional response measure was decline in maximum SUV (SUV_{max}; AUC, 0.76). Two new intensity features, decline in mean SUV (SUV_{mean}) and skewness, and 3 texture features (inertia, correlation, and cluster prominence) were found to be significant predictors with AUC values $\geq$0.76. According to these features, a tumor was more likely to be a responder when the SUV_{mean} decline was larger, when there were relatively fewer voxels with higher SUV values pre-CRT, or when [^{18}F]FDG uptake post-CRT was relatively homogeneous. All of the most accurate predictive features were extracted from the entire tumor rather than from the most active part of the tumor. For SUV intensity features and tumor size features, changes were more predictive than pre- or post-CRT assessment alone.

Conclusion: Spatial-temporal [^{18}F]FDG-PET features were found to be useful predictors of pathologic tumor response to neoadjuvant CRT in esophageal cancer. © 2013 Elsevier Inc.

非结构性摘要

Abstract

Statistical iterative reconstruction algorithms have shown potential to improve cone-beam CT (CBCT) image quality. Most iterative reconstruction algorithms utilize prior knowledge as a penalty term in the objective function. The penalty term greatly affects the performance of a reconstruction algorithm. The total variation (TV) penalty has demonstrated great ability in suppressing noise and improving image quality. However, calculated from the first-order derivatives, the TV penalty leads to the well-known staircase effect, which sometimes makes the reconstructed images oversharpen and unnatural. In this study, we proposed to use a second-order derivative penalty that involves the Frobenius norm of the Hessian matrix of an image for CBCT reconstruction. The second-order penalty retains some of the most favorable properties of the TV penalty like convexity, homogeneity, and rotation and translation invariance, and has a better ability in preserving the structures of gradual transition in the reconstructed images. An effective algorithm was developed to minimize the objective function with the majorization-minimization (MM) approach. The experiments on a digital phantom and two physical phantoms demonstrated the priority of the proposed penalty, particularly in suppressing the staircase effect of the TV penalty.

摘要撰写

写作要求：

- 文摘可单独发表，应有独立性和自明性。
- 结构严谨、语义确切、表达简明；
- 文字简练，约300~500字;
- 不举例证，不用图表；
- 不用非标准术语、缩略语、简称、代号或符号；
- 不使用文章列出的章节号、图号、表号、公式号；
- 不引用参考文献。
- 摘要中所有信息在正文中能找到；

- 背景不能介绍过多，也不能过少；
- 传统写作教程：不使用第一人称（其实也可以）；
- 慎用“重大突破”，”完全解决了”等词汇；
- 避免措辞含糊或不准确；
- 注意摘要中使用合适的专业名词等关键词，以使人通过摘要检索到你的文章；
- 不同专业、不同方向、不同期刊会议的论文写作风格(包括摘要)可能不同，写作前看看相关论文的摘要。

Many analysis-based regularizations proposed so far employ a common prior information, i.e., edges in an image are sparse. However, in local edge regions and texture regions, this prior may not hold. As a result, the performance of regularizations based on the edge sparsity may be unsatisfactory in such regions for image-related inverse problems. These regularizations tend to smooth out the edges while eliminating the noise. In other words, these regularizations' abilities of preserving edges are limited. In this paper, a new prior that the corner points in a natural image are sparse was proposed to construct regularizations. Intuitively, even in local edge regions and texture regions, the sparsity of corner points may still exist, and hence, the regularizations based on it can achieve better performance than those based on the edge sparsity. As an example, by utilizing the sparsity of corner points, we proposed a new regularization based on Noble's corner measure function. Our experiments demonstrated the excellent performance of the proposed regularization for both image denoising and deblurring problems, especially in local edge regions and texture regions.	研究背景 研究问题 研究方法 研究结果

H. Liu and S. Tan, "Image Regularizations Based on the Sparsity of Corner Points," *IEEE Transactions on Image Processing*, vol. 28, pp. 72-87, Jan 2019.

To increase the temporal resolution and maximal imaging time of super-resolution (SR) microscopy, we have developed a deconvolution algorithm for structured illumination microscopy based on Hessian matrixes (Hessian-SIM). It uses the continuity of biological structures in multiple dimensions as a priori knowledge to guide image reconstruction and attains artifact-minimized SR images with less than 10% of the photon dose used by conventional SIM while substantially outperforming current algorithms at low signal intensities. Hessian-SIM enables rapid imaging of moving vesicles or loops in the endoplasmic reticulum without motion artifacts and with a spatiotemporal resolution of 88 nm and 188 Hz. Its high sensitivity allows the use of sub-millisecond excitation pulses followed by dark recovery times to reduce photobleaching of fluorescent proteins, enabling hour-long time-lapse SR imaging of actin (肌动蛋白) filaments in live cells. Finally, we observed the structural dynamics of mitochondrial cristae (线粒体) and structures that, to our knowledge, have not been observed previously, such as enlarged fusion pores during vesicle exocytosis (囊泡胞吐).	研究目的 研究方法 研究结果 新的发现

Huang, X., J. Fan, L. Li, H. Liu, R. Wu, Y. Wu, L. Wei, H. Mao, A. Lal, P. Xi, L. Tang, Y. Zhang, Y. Liu, S. Tan and L. Chen (2018). "Fast, long-term, super-resolution imaging with Hessian structured illumination microscopy." Nature Biotechnology 36: 451-459.

谦虚、谨慎写作

- 写作时夸大其词、狂妄无知，会让人极度反感；慎用“原创”“首创”“首次”“国内领先”“国际领先”“世界水平”“填补重大空白”“重大突破”等词语。
- 一个谦虚的例子：

1831年，法拉第写信给朋友说：我现在又忙着，在研究电磁效应，我觉得自己做出点东西来了，但还没把握。可能是根草，而不是一条鱼，但是，经过这一番努力以后，总算可以拉出来的。

他拉出来的是历史上第一台发电机。

- 确实是首次时，一般使用(经过充分调查后)：

To the best of our knowledge, we are the first …

关键词

Keywords，index terms

- 每篇论文选择3~8个关键词
- 应该是名词、术语、或名词性词组、短语；冠词、介词、连词、代词、情态动词等虚词不能作关键词
- 关键词间，相互空一格书写，不加标点符号或者用 “;” “，”隔开，不用“和”，“与”，“而”等连接。

- 有助于读者迅速了解论文主题信息
- 搜索引擎及数据库检索论文的工具，好的关键词有助于提高检索成功率 (太短的关键字会使搜索变得不明确，而太长的关键字可能会检索不到文章)
- 遵循期刊指南 (例如，某些医学期刊推荐从美国国家医学图书馆的医学主题词（MeSH）集合中提取关键词)
- 测试你的关键词是否合适的一个方法：用搜索引擎试试你的关键词，看看使用这些关键词能否搜索出与你文章相似的文章。

关键词选择：Be specific to your field or sub-field

Manuscript title: Direct observation of nonlinear optics in an isolated carbon nanotube (直接观察孤立的碳纳米管中的非线性光学)

Poor keywords: molecule, optics, lasers, energy lifetime (分子，光学，激光，能量寿命)

Better keywords: single-molecule interaction, Kerr effect, carbon nanotubes, energy level structure (单分子相互作用，克尔效应，碳纳米管，能级结构)

Manuscript title: Increases in levels of sediment transport at former glacial-interglacial transitions (前冰期至冰期间过渡期泥沙输送量增加**)**

Poor keywords: climate change, erosion, plant effects (气候变化，侵蚀，植物效应)

Better keywords: quaternary climate change, soil erosion, bioturbation (第四纪气候变化，土壤侵蚀，生物扰动)

关键词

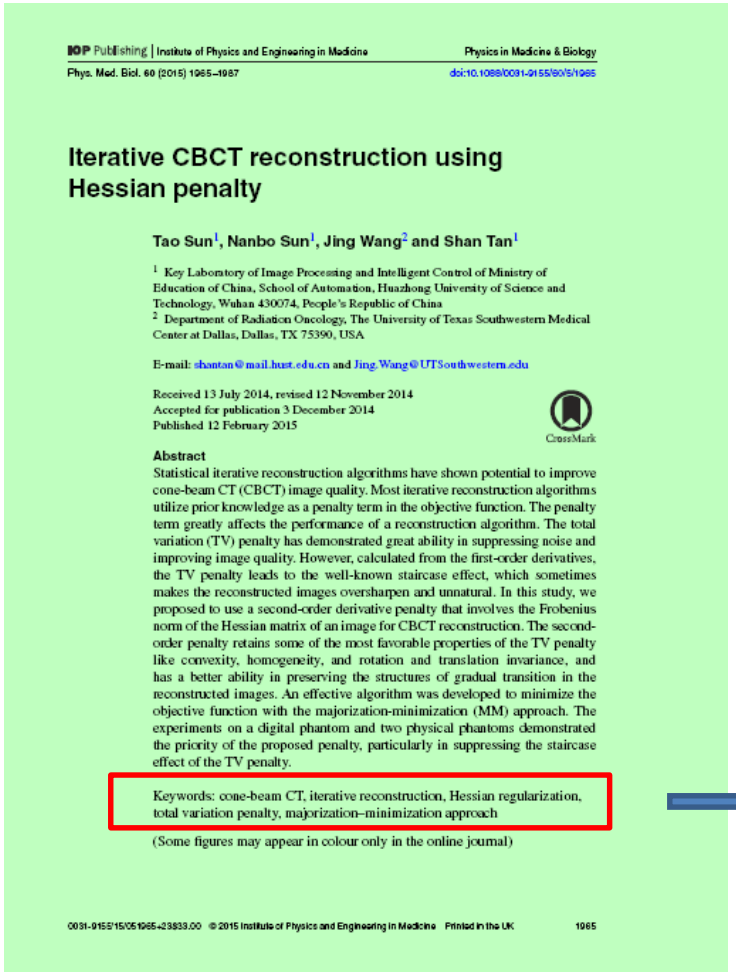

IOP Publishing | Institute of Physics and Engineering in Medicine Physics in Medicine & Biology
Phys. Med. Biol. 60 (2015) 1965–1987 doi:10.1088/0031-9155/60/5/1965

Iterative CBCT reconstruction using Hessian penalty

Tao Sun[1], Nanbo Sun[1], Jing Wang[2] and Shan Tan[1]

[1] Key Laboratory of Image Processing and Intelligent Control of Ministry of Education of China, School of Automation, Huazhong University of Science and Technology, Wuhan 430074, People's Republic of China
[2] Department of Radiation Oncology, The University of Texas Southwestern Medical Center at Dallas, Dallas, TX 75390, USA

E-mail: shantan@mail.hust.edu.cn and Jing.Wang@UTSouthwestern.edu

Received 13 July 2014, revised 12 November 2014
Accepted for publication 3 December 2014
Published 12 February 2015

Abstract

Statistical iterative reconstruction algorithms have shown potential to improve cone-beam CT (CBCT) image quality. Most iterative reconstruction algorithms utilize prior knowledge as a penalty term in the objective function. The penalty term greatly affects the performance of a reconstruction algorithm. The total variation (TV) penalty has demonstrated great ability in suppressing noise and improving image quality. However, calculated from the first-order derivatives, the TV penalty leads to the well-known staircase effect, which sometimes makes the reconstructed images oversharpen and unnatural. In this study, we proposed to use a second-order derivative penalty that involves the Frobenius norm of the Hessian matrix of an image for CBCT reconstruction. The second-order penalty retains some of the most favorable properties of the TV penalty like convexity, homogeneity, and rotation and translation invariance, and has a better ability in preserving the structures of gradual transition in the reconstructed images. An effective algorithm was developed to minimize the objective function with the majorization-minimization (MM) approach. The experiments on a digital phantom and two physical phantoms demonstrated the priority of the proposed penalty, particularly in suppressing the staircase effect of the TV penalty.

Keywords: cone-beam CT, iterative reconstruction, Hessian regularization, total variation penalty, majorization–minimization approach

(Some figures may appear in colour only in the online journal)

Keywords: cone-beam CT, iterative reconstruction, Hessian regularization, total variation penalty, majorization–minimization approach

关键词

2588 IEEE TRANSACTIONS ON MEDICAL IMAGING, VOL. 36, NO. 12, DECEMBER 2017

Low-Dose CBCT Reconstruction Using Hessian Schatten Penalties

Liang Liu, Xinxin Li, Kai Xiang, Jing Wang, and Shan Tan, *Member, IEEE*

***Abstract*— Cone-beam computed tomography (CBCT) has been widely used in radiation therapy. For accurate patient setup and treatment target localization, it is important to obtain high-quality reconstruction images. The total variation (TV) penalty has shown the state-of-the-art performance in suppressing noise and preserving edges for statistical iterative image reconstruction, but it sometimes leads to the so-called staircase effect. In this paper, we proposed to use a new family of penalties—the Hessian Schatten (HS) penalties—for the CBCT reconstruction. Consisting of the second-order derivatives, the HS penalties are able to reflect the smooth intensity transitions of the underlying image without introducing the staircase effect. We discussed and compared the behaviors of several convex HS penalties with orders 1, 2, and + ∞ for CBCT reconstruction. We used the majorization-minimization approach with a primal-dual formulation for the corresponding optimization problem. Experiments on two digital phantoms and two physical phantoms demonstrated the proposed penalty family's outstanding performance over TV in suppressing the staircase effect, and the HS penalty with order 1 had the**

***Index Terms*— CBCT, image reconstruction, TV, staircase effect, Hessian Schatten penalty.**

I. INTRODUCTION

CONE-BEAM computed tomography (CBCT) provides volumetric information for patient setup and target localization during radiation therapy. Repeated CBCT scans during a treatment course expose patients to extra imaging radiation doses [1], [2]. Lowering the mAs (tube current exposure time product) level in CBCT acquisition can reduce the imaging dose and associated risks to patients [3]. However, the quality of the reconstructed low-mAs image can be dramatically degraded due to excessive noise [4], [5].

Statistical iterative reconstruction (SIR) algorithms have been used to improve the quality of low-dose CBCT imaging [6], [7]. Commonly used penalty terms in SIR include the isotropic quadratic penalty [8], the Huber penalty [9], and the total variation (TV) penalty [10]–[12].

Originally introduced for image de-noising by Rudin *et al.* [10], the TV penalty has shown state-of-the-art performance in preserving edges and suppressing noise for CBCT imaging [10]–[24]. Various TV-based CBCT reconstruction algorithms have been studied and evaluated in the last three decades [10]–[24]. Sidky and Pan proposed to minimize the TV penalty subject to a non-negative constraint for sparse-view projection reconstruction, where the TV objective function was minimized by steepest descent with an adaptive step size, and the non-negative constraint was enfor[18]. [17], Tian et al. [20] studied the selection parameter values in the constrained TV minimization-based reconstruction and showed, with both visualization and quantitative assessments, that the reconstructions were greatly improved, relative to the clinical FDK reconstruction, in terms of the devised utility metrics. Bian *et al.* [21] showed that the TV-based iterative algorithm was more robust to different data conditions, such as number of views and exposure levels, than the FDK algorithm for CBCT reconstruction. Hashemi *et al.* [14] proposed a simultaneous deblurring and iterative reconstruction to explicitly account for image unsharpness caused by different factors in the CBCT reconstruction formulation when using the TV penalty. Huang and Hsiao [15] proposed an iterative reconstruction method to accelerate the ordered-subsets reconstruction with a power factor, in combination with the TV minimization method.

The major limitation of the TV penalty is that it sometimes causes the staircase effect in reconstructed images [25], [26], particularly at low-dose levels [16]. TV favors penalizing the first-order derivatives, *i.e.*, minimizing the intensity difference between neighboring pixels. Therefore, it tends to produce piecewise constant reconstructed images, even when the underlying images are not necessarily piecewise constant.

To avoid the staircase effect due to the TV penalty, Yan *et al.* [26] considered the anisotropic edge property

Manuscript received August 7, 2017; revised September 22, 2017; accepted October 15, 2017. Date of publication October 24, 2017; date of current version November 29, 2017. This work was supported by the National Natural Science Foundation of China under Grant 61375018 and Grant 61672253. The work of J. Wang was supported in part by the Cancer Prevention and Research Institute of Texas under Grant RP130109 and Grant RP110562-P2, in part by the National Institute of Biomedical Imaging and Bioengineering under Grant R01 EB020366, and in part by the American Cancer Society under Grant RSG-13-326-01-CCE. *(Corresponding authors: Jing Wang; Shan Tan.)*

L. Liu, X. Li, K. Xiang, and S. Tan are with the Key Laboratory of Image Processing and Intelligent Control of Ministry of Education of China, and the School of Automation, Huazhong University of Science and Technology, Wuhan, Hubei 430074, China (e-mail: liangliu@hust.edu.cn; xxl117@hust.edu.cn; u201314635@hust.edu.cn; shantan@hust.edu.cn).

J. Wang is with the Department of Radiation Oncology, University of Texas Southwestern Medical Center, Dallas, TX 75390 USA (e-mail: jing.wang@utsouthwestern.edu).

Color versions of one or more of the figures in this paper are available online at http://ieeexplore.ieee.org.

Digital Object Identifier 10.1109/TMI.2017.2786185

***Index Terms*— CBCT, image reconstruction, TV, staircase effect, Hessian Schatten penalty.**

前言(Introduction)

介绍论文背景、相关领域研究历史与现状，理论依据的实验基础、论文成果在本领域的地位和作用、本文目的等。

基本内容：

- 目前研究的热点、存在的问题及研究工作的历史背景和引起研究工作进行的缘由(问题的由来)；
- 前人的研究进展(已有实验，已有结果，已明确问题，未解决问题)及最近研究动态(重要文献简述)；
- 强调本研究的重要性、必要性及意义等。
- 点明本文理论依据、实验基础和研究方法，简要阐述研究内容，预示研究结果、意义和前景，但不必展开详细讨论。

Introduction

- A template:

1. Problem X is important
2. A, B, and C have been done
3. A, B, and C have their weakness

Why

4. Our work D

How

5. Features and advantages of D
6. Experimental results of D

What

7. Organization of the paper

Introduction

1. Problem X is important
2. A, B, and C have been done
3. A, B, and C have their weakness

Why

Previous works

Purpose: Why your work, the differences

1. Categorization of previous works
2. One or two sentences for a work
   a. Strength
   b. Weakness
3. Don’t over-criticize previous works
4. Emphasize the difference

1. Introduction

There is growing interest in using the on-board cone-beam computed tomography (CBCT) for image-guided radiation therapy (Jaffray *et al* 2002). A great concern is that the excessive radiation dose due to its repeated use during a treatment course poses potential risk to the health of patients (Islam *et al* 2006, Brenner and Hall 2007). One way to reduce radiation dose is to lower mAs level in CT projection data acquisition. However, excessive quantum noise leads to degraded reconstructed CBCT images (Wang *et al* 2008a), which renders low-mAs CBCT a less attractive option for the therapeutic guidance.

Statistical iterative reconstruction (SIR) algorithms have shown superior performance in improving image quality (Ouyang *et al* 2011). The choice of the penalty term in the objective function greatly affects the quality of the reconstructed images. In the general maximum *a posterior* (MAP) estimate in inverse problems like CBCT reconstruction, the penalty term imposes prior knowledge on the desired results. The Markov random field (MRF) (Geman and Geman 2009) has been widely used and can derive a variety of distinct penalties by choosing different potential functions. One common model is the Gaussian Markov random field (GMRF) (Hanson and Wecksung 1983). However, the Gaussian prior penalty results in excessive noisy or blurred images. Some non-Gaussian distribution function have been used such as the Huber function (Chlewicki *et al* 2004), the log-cosh function (Green 1990) and the Gibbs functions (Lange 1990). Thibault *et al* proposed the *q*-generalized Gaussian Markov random field (*q*-GGMRF) penalty (Thibault *et al* 2007) which generalizes many existing penalties. Other commonly used penalties include the isotropic penalty (Fessler 1994), the anisotropic penalty (Wang *et al* 2008b) and the total variation (TV) penalty (Sidky *et al* 2006, Jia *et al* 2010), etc.

The TV penalty has shown the state-of-the-art performance in suppressing noises and preserving edges (Sidky *et al* 2006, Jia *et al* 2010). Besides, it has been used as the sparsifying transform function in many compress sensing-based reconstruction algorithms (Choi *et al* 2010, Lee *et al* 2012, Park *et al* 2012). The success of the TV penalty lies in its good properties such as simplicity, convexity, and rotation and shift invariance (Boyd and Vandenberghe 2004). These properties make it possible to derive various efficient algorithms. Despite its success, the TV penalty often leads to the well-known staircase effect (Chan *et al* 2000, Yuan *et al* 2009). The reason is that the TV penalty favors minimizing the first-order derivatives and thus tends to have piecewise constant results (Yuan *et al* 2009). This tendency can be highly undesirable in biomedical imaging where the intensity of neighboring tissues usually has gradual transitioning. The staircase effect in the biomedical image may falsely reflect the true structure of the tissues and leads to incorrect interpretation of the images.

In this study, we proposed to use the Hessian penalty for CBCT reconstruction that involves the Frobenius norm of the Hessian matrix of an image to suppress the staircase effect observed in the TV penalty. The Hessian penalty is a second-order derivative penalty. The motivation behind is that the second-order derivatives have a weaker penalty on the absolute difference between neighboring voxels and allow for piecewise smooth reconstructed results, thus better reflecting the natural intensity transition in CBCT images. The Hessian penalty retains most favorable properties of TV such as convexity, homogeneity, rotation and translation invariance (Boyd and Vandenberghe 2004), and have shown improved performance in suppressing the staircase effect and enhancing the image quality for image denoising (Chan *et al* 2000) and microscopy image debluring (Lefkimmiatis *et al* 2012). In previous CBCT reconstruction methods (Fessler 1994, Wang *et al* 2008b), most of the penalty terms are in quadratic form by themselves, and thus the optimization of the associated objective functions can be directly performed by algorithms such as Gauss-Seidel update and conjugate gradient descent. Unfortunately, the Hessian penalty is not

quadratic, which makes the minimization of the objective function challenging. We developed an effective algorithm to minimize the objective function with the majorization-minimization (MM) approach. The objective function was upper-bounded by a sequence of quadratic majorizers, which can be minimized directly using the Gauss-Seidel update strategy. In this way, the optimization problem of the original objective function was converted to a sequence of simple optimization problems. We conducted a systematic comparison on a simulated phantom and two physical phantoms. The results demonstrated that the proposed penalty outperforms the TV penalty, particularly in suppressing the staircase effect. To the best of our knowledge, this is the first time that the Hessian penalty was used in CBCT reconstruction.

2. Mathematical models

2.1. PWLS image reconstruction

The model of x-ray CT data acquisition is based on the line integration along the x-ray path of the tissue attenuation, which can be calculated through the logarithm transform of the ratio of incident and detected photon numbers

$$\bar{p}_i = \ln\frac{I_{i0}}{I_i} = \int_l \mu(x,y,z)\,\mathrm{d}l, \tag{1}$$

where l is the x-ray path, $\bar{p}_i$ is the projection datum corresponding to the path and μ is the linear attenuation coefficient image. The reconstruction is aimed at estimating μ from a series of line integral values, i.e. the observed projection data $\bar{p}$. The statistical noise property of the x-ray CT projection data after logarithm transform approximately follows a Gaussian distribution (Wang *et al* 2008). The variance of the noise at the detector bin i can be estimated as follows:

$$\sigma_i^2 = \exp(\bar{p}_i)/N_{i0}, \tag{2}$$

where N_{i0} is the incident photon number, and $\bar{p}_i$ and σ_i^2 are the mean and variance of projection datum, all at the detector bin i. The reconstruction can be formulated as a minimization problem with the objective function (Wang *et al* 2008b)

$$\Phi(\mu) = \frac{1}{2}(\bar{p} - A\mu)^T \Sigma^{-1}(\bar{p} - A\mu) + \beta R(\mu), \tag{3}$$

where Σ is a diagonal matrix with diagonal element σ_i^2, and A is the projection matrix, in which the element A_{ij} is the intersection length of the ith projection with the image voxel μ_j. The first term in equation (3) is the weighted least-squares (WLS) criterion or a data-fidelity term. The elements of the diagonal matrix Σ play the role of weighting in the WLS cost function and determine the contribution of each measurement. The second term is a prior constraint or a penalty term, where β controls the trade-off between the data-fidelity term and the penalty term. The image reconstruction task is to find an attenuation coefficient image μ by minimizing the objective function with a positive constraint. The method for CBCT reconstruction using equation (3) is referred to as the penalized weighted least-square (PWLS) criterion (Wang *et al* 2008b).

2.2. Hessian penalty

The prior constraint in equation (3) enforces a smoothness penalty on the solution. Minimization of the total variation (TV) of an image has shown good properties in noise suppressing and

Low-Dose CBCT Reconstruction Using Hessian Schatten Penalties

Liang Liu, Xinxin Li, Kai Xiang, Jing Wang, and Shan Tan, *Member, IEEE*

***Abstract*—Cone-beam computed tomography (CBCT) has been widely used in radiation therapy. For accurate patient setup and treatment target localization, it is important to obtain high-quality reconstruction images. The total variation (TV) penalty has shown the state-of-the-art performance in suppressing noise and preserving edges for statistical iterative image reconstruction, but it sometimes leads to the so-called staircase effect. In this paper, we proposed to use a new family of penalties—the Hessian Schatten (HS) penalties—for the CBCT reconstruction. Consisting of the second-order derivatives, the HS penalties are able to reflect the smooth intensity transitions of the underlying image without introducing the staircase effect. We discussed and compared the behaviors of several convex HS penalties with orders 1, 2, and $+\infty$ for CBCT reconstruction. We used the majorization-minimization approach with a primal-dual formulation for the corresponding optimization problem. Experiments on two digital phantoms and two physical phantoms demonstrated the proposed penalty family's outstanding performance over TV in suppressing the staircase effect, and the HS penalty with order 1 had the best performance among the HS penalties tested.**

***Index Terms*—CBCT, image reconstruction, TV, staircase effect, Hessian Schatten penalty.**

I. Introduction

CONE-BEAM computed tomography (CBCT) provides volumetric information for patient setup and target localization during radiation therapy. Repeated CBCT scans during a treatment course expose patients to extra imaging radiation doses [1], [2]. Lowering the mAs (tube current exposure time product) level in CBCT acquisition can reduce the imaging dose and associated risks to patients [3]. However, the quality of the reconstructed low-mAs image can be dramatically degraded due to excessive noise [4], [5].

Statistical iterative reconstruction (SIR) algorithms have been used to improve the quality of low-dose CBCT imaging [6], [7]. Commonly used penalty terms in SIR include the isotropic quadratic penalty [8], the Huber penalty [9], and the total variation (TV) penalty [10]–[12].

Originally introduced for image de-noising by Rudin *et al.* [10], the TV penalty has shown state-of-the-art performance in preserving edges and suppressing noise for CBCT imaging [10]–[24]. Various TV-based CBCT reconstruction algorithms have been studied and evaluated in the last three decades [10]–[24]. Sidky and Pan proposed to minimize the TV penalty subject to a non-negative constraint for sparse-view projection reconstruction, where the TV objective function was minimized by steepest descent with an adaptive step size, and the non-negative constraint was enforced by projection onto convex sets (POCS) [13], [18], [19]. Han *et al.* [20] studied the selection of parameter values in the constrained TV minimization-based reconstruction and showed, with both visualization and quantitative assessments, that the reconstructions were greatly improved, relative to the clinical FDK reconstruction, in terms of the devised utility metrics. Bian *et al.* [21] showed that the TV-based iterative algorithm was more robust to different data conditions, such as number of views and exposure levels, than the FDK algorithm for CBCT reconstruction. Hashemi *et al.* [14] proposed a simultaneous deblurring and iterative reconstruction to explicitly account for image unsharpness caused by different factors in the CBCT reconstruction formulation when using the TV penalty. Huang and Hsiao [15] proposed an iterative reconstruction method to accelerate the ordered-subsets reconstruction with a power factor, in combination with the TV minimization method.

The major limitation of the TV penalty is that it sometimes causes the staircase effect in reconstructed images [25], [26], particularly at low-dose levels [16]. TV favors penalizing the first-order derivatives, *i.e.*, minimizing the intensity difference between neighboring pixels. Therefore, it tends to produce piecewise constant reconstructed images, even when the underlying images are not necessarily piecewise constant.

To avoid the staircase effect due to the TV penalty, Yan *et al.* [26] considered the anisotropic edge property among neighboring image voxels for TV-POCS implementation, where the associated weights were expressed as an exponential function and can be adjusted adaptively by the local image-intensity gradient to preserve the edge details for sparse-view low-dose CT image reconstruction. Several alternative penalty terms with higher-order derivatives have been proposed in other fields, such as image restoration [27] and microscopy imaging deconvolution [28]. These penalty terms do not directly penalize the intensity difference between neighboring pixels. Recently, Sun *et al.* [29] replaced the TV penalty with a Hessian penalty in a CBCT SIR algorithm. The Hessian penalty was constructed using the second-order derivative operations and was defined as the Frobenius norm of the Hessian matrix of the image. They used the majorization-minimization (MM) method for the associated optimization problem. In their algorithm, the objective function was upper-bounded by a sequence of quadratic majorizers, which can be minimized directly using the Gauss-Seidel update strategy [29]. The proposed Hessian penalty proved successful in suppressing the TV penalty's staircase effect. However, like most higher-order penalties, the Hessian penalty tends to slightly blur the edges of the reconstructed image. Shi *et al.* [30] proposed a new penalty combining the TV and Hessian penalties in a structure-adaptive way to reconstruct CBCT images without introducing extra parameters. The proposed penalty can automatically adjust the weight parameters between TV and Hessian according to local image structures to suppress the staircase effect and preserve edges simultaneously.

The Hessian Schatten (HS) penalties are a novel family of second-degree penalties proposed recently by Lefkimmiatis *et al.* [31] to avoid the staircase effect for ill-posed linear inverse problems. The penalties in this family are invariant, convex, and non-quadratic, and they are defined as the Schatten norm of the Hessian matrix of the underlying image at each image point [31]. The Schatten norm is a p-norm of the vector of the singular values of a matrix, including many popular matrix norms, such as the nuclear/trace norm ($p = 1$), the Frobenius norm ($p = 2$), and the spectral/operator norm ($p = \infty$). The HS family generalizes the Hessian penalty and provides a more flexible family of second-order penalties. The Hessian penalty employed by Sun *et al.* [29] is a special case of the HS penalty with $p = 2$. Hu *et al.* showed that the HS penalty with $p = 1$ is nearly proportional to the higher degree total variation (HDTV) penalty with order 2 [32]. The HS family provides a natural way to incorporate image local geometry structure information. Specifically, an HS penalty can be interpreted as a scalar measurement of the curvature at a local image surface patch, and the eigenvalues of the Hessian matrix correspond to the principal curvatures, which can be used to measure the surface flatness in different directions [31].

The selection of the p value can affect the regularized solution when using the HS penalties for ill-posed linear inverse problems. Lefkimmiatis *et al.* showed that, for most cases, the HS penalty with $p = 1$ gives better results than the HS penalties with $p = 2$ and $p = \infty$ in sparse image restoration and microscopy image deburring [31]. Similar phenomena have been observed in both the compressed sensing problem [33] and the rank minimization problem for data recovery in computer vision. It is well-known that finding the sparsest representation (the l_0 norm minimization problem) in compressed sensing [34] and minimizing the data rank for recovering noisy/missing input data are both *NP*-hard [35], [36]. The l_1 norm minimization is known to be the best convex approximation of the l_0 norm minimization problem in compressed sensing among all p's in (0, 2) [34]. Note that the Schatten norm with $p = 0$ (quasinorm) measures the rank of a matrix and thus provides a natural way to approximate the rank minimization problem. Kong *et al.* [37] showed that the Schatten norm gave better approximation results to the rank minimization problem at smaller p values for noisy data recovery.

In this study, we employed the Hessian Schatten (HS) penalty family for 3D CBCT image reconstruction. The purpose of this study was two-fold. First, we designed a new SIR algorithm based on the HS penalty family for CBCT reconstruction to avoid the staircase effect [38]. Second, we compared the behavior and performance of HS penalties with different orders ($p = 1$, $p = 2$, and $p = \infty$) for CBCT reconstruction. We note that the HS penalty is convex with $p \geq 1$ and non-convex (quasinorm) with $0 \leq p < 1$.

One major challenge when using HS penalties for 3D CBCT reconstruction is that members in this penalty family are not smooth and differentiable, which prohibits direct use of a gradient-based method to optimize the objective function. Furthermore, the optimization method proposed by Sun *et al.* [29] cannot be directly generalized to the HS penalties with $p = 1$ and $p = \infty$, as they are both non-quadratic. In this study, we adopted a primal-dual formulation originally proposed by Lefkimmiatis *et al.* [31] for 3D CBCT reconstruction with HS penalties of orders 1, 2, and ∞. The original formulation was proposed in 2D [31], and extending it to 3D is not trivial. For example, in this study, we deduced the numerical formulation of the conjugate Hessian operator in 3D and proved that the dual objective function using the HS penalty for 3D CBCT reconstruction is Lipschitz continuous. We also derived the projection operator onto the l_q unit-ball ($1/p + 1/q = 1$) using an efficient algorithm in 3D [39].

The HS family tends to penalize the second-order derivatives, thus yielding smooth reconstructions, rather than the piecewise constant reconstructions that the TV penalty yields. Therefore, the reconstructed image can more faithfully reflect the real intensity transitions of the underlying image. We compared experiments conducted from simulated projection data and real projection data to demonstrate the effectiveness of the HS penalty family. Our experimental results showed that all the tested HS penalties significantly suppressed the staircase effect, and the HS penalty with $p = 1$ (nuclear/trace norm) performed best in most cases, closely followed by the HS with $p = 2$ (Frobenius norm).

II. Mathematical Modeling

The X-ray CT projection is the line integration along the X-ray path l of the tissue attenuation, which can be calculated as the logarithm transform of the ratio of the incident and

Manuscript received August 7, 2017; revised September 22, 2017; accepted October 15, 2017. Date of publication October 24, 2017; date of current version November 29, 2017. This work was supported by the National Natural Science Foundation of China under Grant 61375018 and Grant 61672253. The work of J. Wang was supported in part by the Cancer Prevention and Research Institute of Texas under Grant RP130109 and Grant RP110562-P2, in part by the National Institute of Biomedical Imaging and Bioengineering under Grant R01 EB020366, and in part by the American Cancer Society under Grant RSG-13-326-01-CCE. *(Corresponding authors: Jing Wang; Shan Tan.)*

L. Liu, X. Li, K. Xiang, and S. Tan are with the Key Laboratory of Image Processing and Intelligent Control of Ministry of Education of China, and the School of Automation, Huazhong University of Science and Technology, Wuhan, Hubei 430074, China (e-mail: liangliu@hust.edu.cn; xxl117@hust.edu.cn; u201314635@hust.edu.cn; shantan@hust.edu.cn).

J. Wang is with the Department of Radiation Oncology, University of Texas Southwestern Medical Center, Dallas, TX 75390 USA (e-mail: jing.wang@utsouthwestern.edu).

Color versions of one or more of the figures in this paper are available online at http://ieeexplore.ieee.org.

Digital Object Identifier 10.1109/TMI.2017.2766185

材料与方法(Materials and methods)

- 论据的主要内容，阐述论点、引出结论的重要部分
- 论文核心，体现作者的创造精神，回答怎么研究（How)
- 论文基础，判断论文科学性、先进性的主要依据

材料与方法

阐述重点(生物、医学类)：

- 实验对象和实验材料性质和特点
- 选取的方法和处理方法
- 实验目的
- 使用的仪器设备和器材
- 实验及测定的方法和过程
- 出现的问题和采取的处理方法

阐述重点(工程、数学类)：

- 问题的本质
- 本文观点，理论或原理分析
- 实现方法或方案
- 数学模型的建立及数学方法的选取
- 定理的证明
- 推导过程
- 物理解释

among neighboring image voxels for TV-POCS implementation, where the associated weights were expressed as an exponential function and can be adjusted adaptively by the local image-intensity gradient to preserve the edge details for sparse-view low-dose CT image reconstruction. Several alternative penalty terms with higher-order derivatives have been proposed in other fields, such as image restoration [27] and microscopy imaging deconvolution [28]. These penalty terms do not directly penalize the intensity difference between neighboring pixels. Recently, Sun *et al.* [29] replaced the TV penalty with a Hessian penalty in a CBCT SIR algorithm. The Hessian penalty was constructed using the second-order derivative operations and was defined as the Frobenius norm of the Hessian matrix of the image. They used the majorization-minimization (MM) method for the associated optimization problem. In their algorithm, the objective function was upper-bounded by a sequence of quadratic majorizers, which can be minimized directly using the Gauss-Seidel update strategy [29]. The proposed Hessian penalty proved successful in suppressing the TV penalty's staircase effect. However, like most higher-order penalties, the Hessian penalty tends to slightly blur the edges of the reconstructed image. Shi *et al.* [30] proposed a new penalty combining the TV and Hessian penalties in a structure-adaptive way to reconstruct CBCT images without introducing extra parameters. The proposed penalty can automatically adjust the weight parameters between TV and Hessian according to local image structures to suppress the staircase effect and preserve edges simultaneously.

The Hessian Schatten (HS) penalties are a novel family of second-degree penalties proposed recently by Lefkimmiatis *et al.* [31] to avoid the staircase effect for ill-posed linear inverse problems. The penalties in this family are invariant, convex, and non-quadratic, and they are defined as the Schatten norm of the Hessian matrix of the underlying image at each image point [31]. The Schatten norm is a p-norm of the vector of the singular values of a matrix, including many popular matrix norms, such as the nuclear/trace norm ($p = 1$), the Frobenius norm ($p = 2$), and the spectral/operator norm ($p = \infty$). The HS family generalizes the Hessian penalty and provides a more flexible family of second-order penalties. The Hessian penalty employed by Sun *et al.* [29] is a special case of the HS penalty with $p = 2$. Hu *et al.* showed that the HS penalty with $p = 1$ is nearly proportional to the higher degree total variation (HDTV) penalty with order 2 [32]. The HS family provides a natural way to incorporate image local geometry structure information. Specifically, an HS penalty can be interpreted as a scalar measurement of the curvature at a local image surface patch, and the eigenvalues of the Hessian matrix correspond to the principal curvatures, which can be used to measure the surface flatness in different directions [31].

The selection of the p value can affect the regularized solution when using the HS penalties for ill-posed linear inverse problems. Lefkimmiatis *et al.* showed that, for most cases, the HS penalty with $p = 1$ gives better results than the HS penalties with $p = 2$ and $p = \infty$ in sparse image restoration and microscopy image deburring [31]. Similar phenomena have been observed in both the compressed sensing problem [33] and the rank minimization problem for data recovery in computer vision. It is well-known that finding the sparsest representation (the l_0 norm minimization problem) in compressed sensing [34] and minimizing the data rank for recovering noisy/missing input data are both *NP*-hard [35], [36]. The l_1 norm minimization is known to be the best convex approximation of the l_0 norm minimization problem in compressed sensing among all p's in (0, 2) [34]. Note that the Schatten norm with $p = 0$ (quasinorm) measures the rank of a matrix and thus provides a natural way to approximate the rank minimization problem. Kong *et al.* [37] showed that the Schatten norm gave better approximation results to the rank minimization problem at smaller p values for noisy data recovery.

In this study, we employed the Hessian Schatten (HS) penalty family for 3D CBCT image reconstruction. The purpose of this study was two-fold. First, we designed a new SIR algorithm based on the HS penalty family for CBCT reconstruction to avoid the staircase effect [38]. Second, we compared the behavior and performance of HS penalties with different orders ($p = 1$, $p = 2$, and $p = \infty$) for CBCT reconstruction. We note that the HS penalty is convex with $p \geq 1$ and non-convex (quasinorm) with $0 \leq p < 1$.

One major challenge when using HS penalties for 3D CBCT reconstruction is that members in this penalty family are not smooth and differentiable, which prohibits direct use of a gradient-based method to optimize the objective function. Furthermore, the optimization method proposed by Sun *et al.* [29] cannot be directly generalized to the HS penalties with $p = 1$ and $p = \infty$, as they are both non-quadratic. In this study, we adopted a primal-dual formulation originally proposed by Lefkimmiatis *et al.* [31] for 3D CBCT reconstruction with HS penalties of orders 1, 2, and ∞. The original formulation was proposed in 2D [31], and extending it to 3D is not trivial. For example, in this study, we deduced the numerical formulation of the conjugate Hessian operator in 3D and proved that the dual objective function using the HS penalty for 3D CBCT reconstruction is Lipschitz continuous. We also derived the projection operator onto the l_q unit-ball ($1/p + 1/q = 1$) using an efficient algorithm in 3D [39].

The HS family tends to penalize the second-order derivatives, thus yielding smooth reconstructions, rather than the piecewise constant reconstructions that the TV penalty yields. Therefore, the reconstructed image can more faithfully reflect the real intensity transitions of the underlying image. We compared experiments conducted from simulated projection data and real projection data to demonstrate the effectiveness of the HS penalty family. Our experimental results showed that all the tested HS penalties significantly suppressed the staircase effect, and the HS penalty with $p = 1$ (nuclear/trace norm) performed best in most cases, closely followed by the HS with $p = 2$ (Frobenius norm).

II. Mathematical Modeling

The X-ray CT projection is the line integration along the X-ray path l of the tissue attenuation, which can be calculated as the logarithm transform of the ratio of the incident and detected intensities [7]:

$$v = \ln \frac{I_0}{I} = \int_l u(x, y, z) dl, \tag{1}$$

where v is the projection, and u is the attenuation coefficient. The noise of the X-ray CT projection approximately follows a Gaussian distribution [6], [7]. The noise variance σ_i^2 associated with the projection v_i at the ith detector bin, can be determined as follows [7]:

$$\sigma_i^2 = \exp(\bar{v}_i)/I_0, \tag{2}$$

where I_0 is the incident photon number, and $\bar{v}_i$ is the mean value of the projection data. The CBCT reconstruction seeks the optimal solution by minimizing the objective function [40]:

$$\Phi(u) = \frac{1}{2}(v - Au)^T \Sigma^{-1}(v - Au) + \tau R(u), \tag{3}$$

where $\tau \geq 0$ is the regularization parameter, A is the system projection matrix, and Σ is a diagonal matrix with its ith element σ_i^2. (Generally, the mean projection $\bar{v}_i$ is not available in practice. To calculate σ_i^2, $\bar{v}_i$ is commonly replaced with the projection v_i, without considering the statistical variation).

A. Hessian Schatten Penalty

In this study, the HS penalty constructed from the second-order derivatives is defined as [31]:

$$R(u) = \|Hu\|_{1,p} = \sum_{i=1}^{N} \|Hu_i\|_{S_p} \quad \forall p \geq 1, \tag{4}$$

where

$$Hu_i = \begin{pmatrix} u^i_{xx} & u^i_{xy} & u^i_{xz} \\ u^i_{yx} & u^i_{yy} & u^i_{yz} \\ u^i_{zx} & u^i_{zy} & u^i_{zz} \end{pmatrix}, \tag{5}$$

H refers to the Hessian operator, N stands for the number of image pixels, $\|\cdot\|_{S_p}$ denotes the Schatten norm of order p (S_p norm) of a matrix, and $\|\cdot\|_{1,p}$ stands for the mixed $l_1 - S_p$ norm. The S_p norm of an $m \times n$ matrix $X \in R^{m \times n}$ is defined as [41]:

$$\|X\|_{S_p} = \left(\sum_{i=1}^{\min(m,n)} \sigma_i^p(X) \right)^{1/p}, \tag{6}$$

where $\sigma_i(X)$ denotes the ith singular value of X. Note that for $0 < p < 1$, $\|X\|_{S_p}$ is a quasinorm. Intuitively, when $p = 0$, the S_p norm measures the rank of the matrix X. The Schatten norm provides an approximation to the rank minimization problem.

After substituting the penalty term in the objective function (3) with the HS penalty defined in Eq.(4), we can rewrite the objective function (3) as:

$$\begin{aligned} \Phi(u) &= \frac{1}{2}(v - Au)^T \Sigma^{-1}(v - Au) + \tau \|Hu\|_{1,p} \\ &= \frac{1}{2}(v - Au)^T \Sigma^{-1}(v - Au) + \tau \sum_{i=1}^{N} \|Hu_i\|_{S_p}. \end{aligned} \tag{7}$$

In this study, we focused on three convex HS penalties with $p = 1, 2$, and ∞.

B. Calculating the Projection Matrix A

To implement a forward projector more efficiently, we adopted the separable footprint (SF) projectors [42]. One of the SF projectors, SF-TR, approximates the voxel footprint functions as 2D separable functions and uses a trapezoid function in the transaxial direction and rectangular functions in the axial direction.

III. Optimizing the Objective Function

A. Reconstruction Process

Our aim in this study is to minimize the objective function (7), in which the HS penalty term is convex but non-smooth.

The first step of the optimization process was to use the MM approach to generate a sequence of upper-bounded functions (9) of the objective function (7). In step 2, we used a primal-dual method to convert the minimization of an upper-bounded function (primal problem) to the maximization of the dual objective function (21) (dual problem). Note that the dual objective function (21) is convex and smooth. In step 3, we solved the dual problem using the Nesterov algorithm [43]. In step 4, we obtained the minimizer of the upper-bounded function from the result of the dual problem through a projection operation (22). To speed up the convergence in each iteration of the MM method, we adopted MFISTA, an extended Nesterov algorithm, to handle a convex non-smooth minimization problem proposed by Beck and Teboulle [44]. Fig. 1 summarizes the optimization process.

B. MM Approach

The main idea of the majorization-minimization (MM) approach is to find the solution by minimizing a sequence of surrogate functions that upper-bound the original objective function (7) [45]. The original objective function is convex, and the solution obtained by minimizing these surrogate majorizer functions will converge to the minimization of the original objective function (7).

To construct the surrogate majorizers of the objective function (7), we defined a function that measures the distance between u and u_t:

$$d(u, u_t) = \frac{1}{2}(u - u_t)^T \left(\alpha I - A^T \Sigma^{-1} A \right)(u - u_t), \tag{8}$$

where t represents the number of iterations. Note that, when $\alpha \geq \|A^T \Sigma^{-1} A\|$, $\alpha I - A^T \Sigma^{-1} A$ is positive definite, and thus $d(u, u_t)$ is non-negative. We obtained the upper-bounded functions (ignoring the constant part) by adding the distance function (8) to the objective function (7):

$$\begin{aligned} Q(u|u_t) &= \Phi(u) + d(u, u_t) = \frac{\alpha}{2}\|u - z\|_2^2 + \tau \|Hu\|_{1,p} \\ &= \frac{1}{2}\|u - z\|_2^2 + \tau \|Hu\|_{1,p} = \frac{1}{2}\|u - z\|_2^2 \\ &\quad + \tau \sum_{i=1}^{N} \|Hu_i\|_{S_p}, \end{aligned} \tag{9}$$

where $z = u_t + \alpha^{-1} A^T \Sigma^{-1}(v - Au_t)$. In the iterative process of minimizing $Q(u|u_t)$, the value of the objective function $\Phi(u)$ kept monotonically non-increasing (Appendix A).

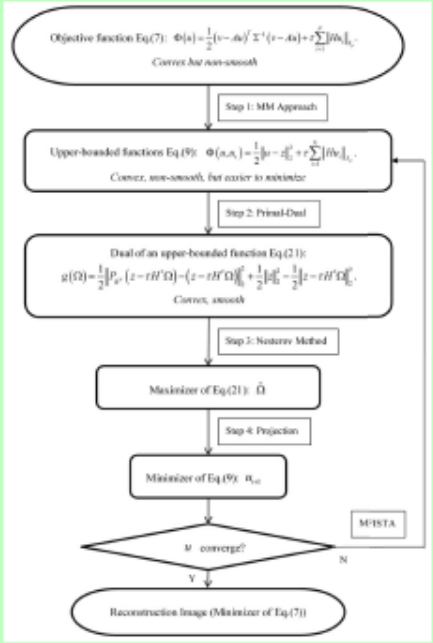

Fig. 1. Main procedure to optimize the objective function.

If $\Phi(u)$ is convex, u_t will converge to the minimizer of $\Phi(u)$. We minimized the objective function (7) by iteratively minimizing the function (9) through the MM method to reconstruct the underlying image.

C. Primal-Dual Method

The fidelity term in (9) is continuously differentiable, while the penalty term is convex but still non-smooth. Because of the relation between the original norm and its dual norm [31], [46], we wrote the equivalent form of the penalty term in (9) as

$$\|Hu\|_{1,p} = \max_{\Omega \in B_{\infty,q}} \langle \Omega, Hu \rangle_{R^{N\times 3\times 3}}, \tag{10}$$

where $1/p + 1/q = 1$, and $B_{\infty,q}$ denotes a unit-norm ball defined as

$$B_{\infty,q} = \left\{ \Omega = \left[\Omega_1^T, \Omega_2^T, \cdots, \Omega_N^T\right]^T \in C^{N\times 3\times 3} : \|\Omega_n\|_{S_q} \le 1, \forall n = 1, 2, \cdots, N \right\}. \tag{11}$$

Let $H*$ represent the conjugate of the Hessian operator H, *i.e.*,

$$\langle \Omega, Hu \rangle_{R^{N\times 3\times 3}} = \langle H^*\Omega, u \rangle_{R^N}. \tag{12}$$

Lefkimmiatis *et al.* [31] deduced the numerical implementation of the conjugate operator $H*$ of the Hessian operator H in 2D. In our study of 3D CBCT construction, where $\Omega \in R^{N\times 3\times 3}$, the conjugate operator $H*$ was quite different than in 2D [31]. To obtain $H*$ in 3D, we rewrote (12) in the following form:

$$\sum_{i=1}^{N} tr\left(\Omega_i (Hu)_i\right) = \sum_{i=1}^{N} u_i \left(H^*\Omega\right)_i. \tag{13}$$

where $tr(\cdot)$ denotes the matrix trace. By expanding the left hand side of (13), we obtained

$$\begin{aligned}
&\sum_{i=1}^{N} tr\left(\Omega_i (Hu)_i\right) \\
&= \sum_{i=1}^{N} u_i \Big(\left(\Delta_{xx}^{(1,1)} \Omega_i^{(1,1)}\right)_i + \left(\Delta_{yy}^{(2,2)} \Omega_i^{(2,2)}\right)_i + \left(\Delta_{zz}^{(3,3)} \Omega_i^{(3,3)}\right)_i \\
&\quad + \left(\Delta_{xy}^{(1,2)} \left(\Omega_i^{(1,2)} + \Omega_i^{(2,1)}\right)\right)_i + \left(\Delta_{xz}^{(1,3)} \left(\Omega_i^{(1,3)} + \Omega_i^{(3,1)}\right)\right)_i \\
&\quad + \left(\Delta_{yz}^{(2,3)} \left(\Omega_i^{(2,3)} + \Omega_i^{(3,2)}\right)\right)_i \Big).
\end{aligned} \tag{14}$$

where Δ_{xx}, Δ_{yy}, Δ_{zz}, Δ_{xy}, Δ_{xz} and Δ_{yz} denote the forward difference operators. By comparing the right hand side of (14) with the right hand side of (13), we obtained the conjugate operator $H*$ of the Hessian operator H for 3D CBCT reconstruction:

$$\begin{aligned}
\left(H^*\Omega\right)_i &= \left(\Delta_{xx}^* \Omega^{(1,1)}\right)_i + \left(\Delta_{yy}^* \Omega^{(2,2)}\right)_i \\
&\quad + \left(\Delta_{xy}^* \left(\Omega^{(1,2)} + \Omega^{(2,1)}\right)\right)_i \\
&\quad + \left(\Delta_{xz}^* \Omega^{(3,3)}\right)_i + \left(\Delta_{xz}^* \left(\Omega^{(1,3)} + \Omega^{(3,1)}\right)\right)_i \\
&\quad + \left(\Delta_{yz}^* \left(\Omega^{(2,3)} + \Omega^{(3,2)}\right)\right)_i,
\end{aligned} \tag{15}$$

where Δ_{xx}^*, Δ_{yy}^*, Δ_{zz}^*, Δ_{xy}^*, Δ_{xz}^*, and Δ_{yz}^* denote the backward difference operators.

We rewrote the penalty term in (9) as:

$$\|Hu\|_{1,p} = \max_{\Omega \in B_{\infty,q}} \langle \Omega, Hu \rangle_{R^{N\times 3\times 3}} = \max_{\Omega \in B_{\infty,q}} \langle H^*\Omega, u \rangle_{R^N}. \tag{16}$$

Replacing the penalty term with its equivalent form (16), the objective function (9) can be written as:

$$\hat{u} = \arg\min_{u \in R^N} \frac{1}{2} \|u - z\|_2^2 + \tau \max_{\Omega \in B_{\infty,q}} \langle H^*\Omega, u \rangle. \tag{17}$$

Using (17), the reconstruction problem became the following min-max problem:

$$\min_{u \in R^N} \max_{\Omega \in B_{\infty,q}} \frac{1}{2} \|u - z\|_2^2 + \tau \langle H^*\Omega, u \rangle. \tag{18}$$

Let $f(u, \Omega) = \frac{1}{2}\|u - z\|_2^2 + \tau \langle H^*\Omega, u \rangle$. Note that $f(u, \Omega)$ is convex in u and concave in Ω, and the order of the minimum and maximum of (18) does not affect the solution [31]. We defined the primal objective function $s(u)$ as

$$s(u) = \max_{\Omega \in B_{\infty,q}} f(u, \Omega) = \frac{1}{2}\|u - z\|_2^2 + \tau \|Hu\|_{1,p}, \tag{19}$$

and the dual objective function as

$$g(\Omega) = \min_{u \in R^N} f(u, \Omega) = \min_{u \in R^N} \frac{1}{2}\|u - z\|_2^2 + \tau \langle H^*\Omega, u \rangle. \tag{20}$$

Letting the gradient $\frac{\partial \frac{1}{2}\|u-z\|_2^2 + \tau \langle H^*\Omega, u \rangle}{\partial u} = u - z + \tau H^*\Omega = 0$, we obtained $u = P_{R^N}(z - \tau H^*\Omega)$, where P_{R^N} was the projection operator onto the set R^N. It followed that

$$\begin{aligned}
g(\Omega) &= \min_{u \in R^N} \frac{1}{2}\|u - (z - \tau H^*\Omega)\|_2^2 + \frac{1}{2}\|z\|_2^2 \\
&\quad - \frac{1}{2}\|z - \tau H^*\Omega\|_2^2 \\
&= \frac{1}{2}\left\|P_{R^N}(z - \tau H^*\Omega) - (z - \tau H^*\Omega)\right\|_2^2 \\
&\quad + \frac{1}{2}\|z\|_2^2 - \frac{1}{2}\|z - \tau H^*\Omega\|_2^2.
\end{aligned} \tag{21}$$

We can calculate the optimal solution $\hat{u}$ of the primal objective function (19) or (9), as long as we have obtained the optimal solution $\hat{\Omega}$ of the dual objective function (21) using the relation of the saddle-value $(\hat{u}, \hat{\Omega})$:

$$\hat{u} = P_{R^N}\left(z - \tau H^*\hat{\Omega}\right). \tag{22}$$

The next step is to calculate the optimal solution $\hat{\Omega}$ by optimizing the dual objective function (21).

D. Nesterov Algorithm

Nesterov [47] introduced a method that achieves a greater convergence rate than the theoretical convergence rate of the classical gradient projection method [43]. We utilized the Nesterov algorithm to optimize the dual objective function (21).

Let P_E denote the projection onto a set E. For the problem of $\min f(x)$ where $x \in E$, if ∇f is Lipschitz continuous with a Lipschitz constant L, the Nesterov algorithm can be summarized as follows [43]:

1. $x_t = P_E\left(y_{t-1} + \nabla f(y_{t-1})/L\right)$,
2. $k_t = \left(1 + \sqrt{1 + 4k_{t-1}^2}\right)/2$,
3. $y_t = x_{t-1} + \left((k_{t-1} - 1)/k_t\right)(x_t - x_{t-1})$.

To utilize the Nesterov algorithm, we first proved that $\nabla g(\Omega)$ is Lipschitz continuous for 3D CBCT reconstruction in Lemma 1 (Appendix B). The dual objective function $g(\Omega)$ is smooth and differentiable in Ω. The gradient of $g(\Omega)$ is

$$\nabla g(\Omega) = \tau H P_{R^N}\left(z - \tau H^*\Omega\right). \tag{23}$$

Lemma 1: For 3D CBCT reconstruction, the dual objective function (21) is Lipschitz continuous, namely,

$$\left\|\nabla g(\Omega) - \nabla g\left(\hat{\Omega}\right)\right\| \le \tau^2 \|H\|^2 \left\|\Omega - \hat{\Omega}\right\|_{R^{N\times 3\times 3}} \le 144\tau^2. \tag{24}$$

To optimize (21) using the Nesterov algorithm, we used the reconstruction image generated by FDK as the initial value.

E. Orthogonal Projections

To construct the penalty term of the objective function, we selected the three commonly used Schatten norms: the Schatten nuclear norm ($p = 1$), the Schatten Frobenius norm ($p = 2$), and the Schatten spectral norm ($p = \infty$). To optimize the dual objective function (21) using the Nesterov algorithm, we needed to calculate the orthogonal projection of a matrix $X \in R^{3\times 3}$ onto the set $B_{S_q} = \left\{X \in R^{3\times 3} : \|X\|_{S_q} \le 1\right\}$. (Note that $1/p + 1/q = 1$. Please see (11)). For a matrix X with singular value decomposition, $U\left[diag\left(\sigma(X)\right)\right]V^T$, its orthogonal projection to B_{S_q} can be expressed as [31]:

$$P_{B_{S_q}}(X) = U\left[diag\left(P_{B_q}\left(\sigma(X)\right)\right)\right]V^H, \tag{25}$$

where $\sigma(X)$ denotes the singular value of the matrix X, $diag(\cdot)$ maps a vector to a diagonal matrix, and P_{B_q} is the orthogonal projection onto the l_q unit-norm ball $B_q = \left\{x \in R_+^{\min(m,n)} : \|x\|_q \le 1\right\}$. According to (25), the orthogonal projection of a matrix in $R^{3\times 3}$ onto the S_q norm ball converts to compute the orthogonal projection of its singulars onto the corresponding l_q unit-norm ball.

In the case of $q = 1$ (corresponding to the Schatten spectral norm ($p = \infty$)), for 3D CBCT image reconstruction, the orthogonal projection of a matrix $X \in R^{3\times 3}$ onto the B_{S_1} unit-norm ball is quite different than that in 2D [31]. In this study, we adopted an efficient algorithm [39] for the projection. The orthogonal projection for $q = 1$ in 3D can be given as (Appendix C):

$$P_{B_{S_1}}(\Omega_n) = U\left[diag\left(S_\gamma\left(\sigma(\Omega_n)\right)\right)\right]V^H, \tag{26}$$

where $S_\gamma(x) = \max(x - \gamma, 0)$ with a threshold

$$\gamma = \begin{cases}
0, & if\ \sigma_1(\Omega_i) + \sigma_2(\Omega_i) + \sigma_3(\Omega_i) \le 1, \\
\dfrac{\left(\sigma_1(\Omega_i) + \sigma_2(\Omega_i) + \sigma_3(\Omega_i) - 1\right)}{3}, & \\
\quad if\ \left(\sigma_1(\Omega_i) + \sigma_2(\Omega_i) + \sigma_3(\Omega_i) > 1\right. & \\
\quad \left.and\ \sigma_1(\Omega_i) + \sigma_2(\Omega_i) - 2\sigma_3(\Omega_i) < 1\right) & \\
\dfrac{\left(\sigma_1(\Omega_i) + \sigma_2(\Omega_i) - 1\right)}{2}, & \\
\quad if\ \left(\sigma_1(\Omega_i) + \sigma_2(\Omega_i) + \sigma_3(\Omega_i) > 1\right. & \\
\quad and\ \sigma_1(\Omega_i) + \sigma_2(\Omega_i) - 2\sigma_3(\Omega_i) \ge 1 & \\
\quad \left.and\ \sigma_1(\Omega_i) - \sigma_2(\Omega_i) < 1\right) & \\
max\left(\sigma_1(\Omega_i), \sigma_2(\Omega_i), \sigma_3(\Omega_i)\right) - 1, & \\
\quad if\ \left(\sigma_1(\Omega_i) + \sigma_2(\Omega_i) + \sigma_3(\Omega_i) > 1\right. & \\
\quad and\ \sigma_1(\Omega_i) + \sigma_2(\Omega_i) - 2\sigma_3(\Omega_i) \ge 1 & \\
\quad \left.and\ \sigma_1(\Omega_i) - \sigma_2(\Omega_i) \ge 1\right). &
\end{cases} \tag{27}$$

In the case of $q = 2$ (corresponding to the Schatten Frobenius norm ($p = 2$)), finding the projection of a matrix $X \in R^{3\times 3}$ onto the B_{S_2} unit-norm ball requires finding a point in the ball that has the shortest distance to the matrix. If the matrix lies inside the B_{S_2} unit-norm ball, the projection is simply itself. Otherwise, the projection is the normalization of the matrix itself. Therefore, we had

$$P_{B_2}(\Omega_i) = \begin{cases} \Omega_i, & if\ \|\Omega_i\|_F \le 1 \\ \dfrac{\Omega_i}{\|\Omega_i\|_F}, & if\ \|\Omega_i\|_F > 1 \end{cases}, \quad i = 1, \ldots, N. \tag{28}$$

where $\|\cdot\|_F$ is the Frobenius norm of a matrix.

In the case of $q = \infty$ (corresponding to the Schatten nuclear norm ($p = 1$)), the orthogonal projection of a matrix $X \in R^{3\times3}$ onto the B_{S_∞} unit-norm ball is similar to the projection onto the B_{S_2} unit-norm ball. The projection can be divided into two cases: inside the B_{S_∞} unit-norm ball and outside the B_{S_∞} unit-norm ball. Different locations correspond to different projection results. Projection onto the B_{S_∞} unit-norm ball can be given as

$$P_{B_{S_\infty}}(\Omega_i) = U\left[diag\left(min\left(\sigma\left(\Omega_i\right), 1\right)\right)\right]V^H, \quad (29)$$

where $\sigma(\Omega_i)$ denotes the singular value of Ω_i, and the $min(\cdot)$ operation compares each of the three singular values with 1 and takes the smaller one.

The pseudo-code of the proposed CBCT reconstruction algorithm using the HS penalties is shown in Appendix D.

IV. Materials and Evaluation

Experiments were conducted on two computer simulation phantoms and two physical phantoms. We used the peak signal to noise ratio (PSNR), the improvement signal to noise ratio (ISNR), the contrast-to-noise ratio (CNR), the structural similarity (SSIM), and the full width at half maximum (FWHM) to quantify the quality of the reconstructed images using different penalty terms [29].

A. Synthetic Phantom

We used two computer simulation phantoms in this study: a Compressed Sensing (CS) phantom [48] and a modified Shepp-Logan phantom. For the CS phantom, we used 360 projections, each containing 800 × 200 pixels, and the pixel size was 0.776 × 0.776 mm^2. For the modified Shepp-Logan phantom, we used 360 projections, each containing 500 × 500 pixels, and the pixel size was 0.776 × 0.776 mm^2. For both phantoms, the source-to-axial distance was 100 cm, and the source-to-detector distance was 150 cm. The incident photon number for the CS phantom was set to be 1×10^3 and 5×10^3 to simulate low-dose and high-dose protocols, respectively. The incident photon number for the Shepp-Logan phantom was set to be 1×10^4, and the noise level was fixed. For both phantoms, the reconstructed image had 350 × 350 × 16 pixels with a pixel size of 0.776 × 0.776 × 0.776 mm^3.

B. Physical Phantom

We used two physical phantoms in this study: a commercial calibration phantom CatPhan 600 (The Phantom Laboratory, Inc., Salem, NY) and an anthropomorphic head phantom. The projections were acquired by the ExactArms (kV source/detector arms) of a Trilogy treatment system (Varian Medical Systems, Palo Alto, CA). The number of projections for a full 360° rotation was 634. The dimensions of each acquired projection were 397 × 298 mm^2, containing 1024 × 768 pixels. For each phantom, the X-ray tube current was set at 10 mA (low-dose) and 80 mA (high-dose) during projection data acquisitions. In both phantom studies, the tube voltage was set at 125 kVp, and the duration of the X-ray pulse at each projection scan was 10 ms. The projection data were acquired in full-fan mode with a bowtie filter. The source-to-axial distance was 100 cm, and the source-to-detector distance was 150 cm. The sizes of the reconstructed image were 350 × 350 × 16 and 550 × 550 × 32 for the CatPhan 600 and anthropomorphic head phantoms, respectively. The sizes of the reconstructed image were 0.776 × 0.776 × 0.776 mm^3 and 0.388 × 0.388 × 0.388 mm^3, respectively.

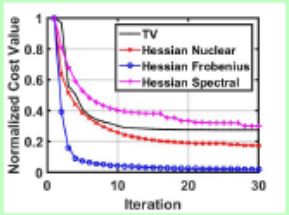

Fig. 2. Convergence curves of the reconstruction algorithms on the CatPhan 600 phantom using TV, HS_1, HS_F, and HS_∞. 'Ratio' is the normalized objective function value.

V. Experimental Results

A. Parameters Setting

CBCT reconstruction always involves a trade-off between image resolution and noise level. Most evaluation criteria used in this work were related to the noise level. To compare the performance of different penalties, we adjusted the parameter τ in Eq. (3) for each phantom by trial and error so that the reconstruction results had the same noise level in each comparison group [40].

To determine the value of α in Eq.(9), we calculated the value of $\left\|A^T\Sigma^{-1}A\right\|$ for each tested phantom and found that setting α to be 2×10^{10} was enough to assure that $\alpha I - A^T\Sigma^{-1}A$ is positive definite for all phantoms in our experiment.

In all iterative reconstruction algorithms, the attenuation coefficient u was initialized using the FDK reconstruction u_0.

B. Convergence Analysis

The range of the values of objective functions using different penalties can differ significantly, even when using exactly the same regularization parameter τ. To make these objective functions "comparable" in the same plot, we used a normalized objective cost to indicate the convergence of the reconstruction algorithms. The normalized objective cost was defined as the ratio of the objective function value of the reconstruction at the kth iteration and that of the initial reconstruction (using FDK), *i.e.* $\Phi(u_k)/\Phi(u_0)$.

To distinguish between different HS penalty terms, we referred to them as HSp, with p denoting the order of the Schatten norm. HS_1, HS_F, and HS_∞ denoted Hessian nuclear ($p = 1$), Hessian Frobenius ($p = 2$), and Hessian spectral norms ($p = \infty$), respectively. Fig. 2 shows the convergence curves of reconstruction methods with TV, HS_∞, HS_1, and HS_F, for the CatPhan 600 phantom. Note that the reconstruction method used for TV is the MM method

实验

- 全文的结论由此得出，讨论由此引发，判断推理和建议由此导出；
- 结果常用精选过的图、表来表示，简洁明了，易于比较，便于观察和记忆。

实验

In the case of $q = \infty$ (corresponding to the Schatten nuclear norm ($p = 1$)), the orthogonal projection of a matrix $X \in R^{3\times3}$ onto the B_{S_∞} unit-norm ball is similar to the projection onto the B_{S_2} unit-norm ball. The projection can be divided into two cases: inside the B_{S_∞} unit-norm ball and outside the B_{S_∞} unit-norm ball. Different locations correspond to different projection results. Projection onto the B_{S_∞} unit-norm ball can be given as

$$P_{B_{S_\infty}}(\Omega_t) = U\left[diag\left(min\left(\sigma\left(\Omega_t\right), 1\right)\right)\right]V^H, \quad (29)$$

where $\sigma(\Omega_t)$ denotes the singular value of Ω_t, and the $min(\cdot)$ operation compares each of the three singular values with 1 and takes the smaller one.

The pseudo-code of the proposed CBCT reconstruction algorithm using the HS penalties is shown in Appendix D.

IV. Materials and Evaluation

Experiments were conducted on two computer simulation phantoms and two physical phantoms. We used the peak signal to noise ratio (PSNR), the improvement signal to noise ratio (ISNR), the contrast-to-noise ratio (CNR), the structural similarity (SSIM), and the full width at half maximum (FWHM) to quantify the quality of the reconstructed images using different penalty terms [29].

A. Synthetic Phantom

We used two computer simulation phantoms in this study: a Compressed Sensing (CS) phantom [48] and a modified Shepp-Logan phantom. For the CS phantom, we used 360 projections, each containing 800 × 200 pixels, and the pixel size was 0.776 × 0.776 mm². For the modified Shepp-Logan phantom, we used 360 projections, each containing 500 × 500 pixels, and the pixel size was 0.776 × 0.776 mm². For both phantoms, the source-to-axial distance was 100 cm and the source-to-detector distance was 150 cm. The incident photon number for the CS phantom was set to be 1×10^5 and 5×10^5 to simulate low-dose and high-dose protocols respectively. The incident photon number for the Shepp-Logan phantom was set to be 1×10^4, and the noise level was fixed. For both phantoms, the reconstructed image had 350 × 350 × 16 pixels with a pixel size of 0.776 × 0.776 × 0.776 mm³.

B. Physical Phantom

We used two physical phantoms in this study: a commercial calibration phantom CatPhan 600 (The Phantom Laboratory, Inc., Salem, NY) and an anthropomorphic head phantom. The projections were acquired by the ExactArms (kV source-detector arms) of a Trilogy treatment system (Varian Medical Systems, Palo Alto, CA). The number of projections for a full 360° rotation was 634. The dimensions of each acquired projection were 397 × 298 mm², containing 1024 × 768 pixels. For each phantom, the X-ray tube current was set at 10 mA (low-dose) and 80 mA (high-dose) during projection data acquisitions. In both phantom studies, the tube voltage was set at 125 kVp, and the duration of the X-ray pulse at each projection scan was 10 ms. The projection data were acquired in full-fan mode with a bowtie filter. The source-to-axial distance was 100 cm, and the source-to-detector distance was 150 cm. The sizes of the reconstructed image were 350 × 350 × 16 and 550 × 550 × 32 for the CatPhan 600 and anthropomorphic head phantoms, respectively. The sizes of the reconstructed image were 0.776 × 0.776 × 0.776 mm³ and 0.388 × 0.388 × 0.388 mm³, respectively.

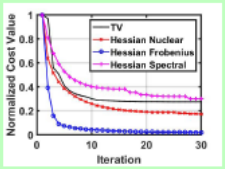

Fig. 2. Convergence curves of the reconstruction algorithms on the CatPhan 600 phantom using TV, HS_1, HS_F, and HS_∞. 'Ratio' is the normalized objective function value.

V. Experimental Results

A. Parameters Setting

CBCT reconstruction always involves a trade-off between image resolution and noise level. Most evaluation criteria used in this work were related to the noise level. To compare the performance of different penalties, we adjusted the parameter τ in Eq. (3) for each phantom by trial and error so that the reconstruction results had the same noise level in each comparison group [40].

To determine the value of α in Eq.(9), we calculated the value of $\left\|A^T\Sigma^{-1}A\right\|$ for each tested phantom and found that setting α to be 2×10^{10} was enough to assure that $\alpha I - A^T\Sigma^{-1}A$ is positive definite for all phantoms in our experiment.

In all iterative reconstruction algorithms, the attenuation coefficient u was initialized using the FDK reconstruction u_0.

B. Convergence Analysis

The range of the values of objective functions using different penalties can differ significantly, even when using exactly the same regularization parameter τ. To make these objective functions "comparable" in the same plot, we used a normalized objective cost to indicate the convergence of the reconstruction algorithms. The normalized objective cost was defined as the ratio of the objective function value of the reconstruction at the kth iteration and that of the initial reconstruction (using FDK), *i.e.* $\Phi(u_k)/\Phi(u_0)$.

To distinguish between different HS penalty terms, we referred to them as HSp, with p denoting the order of the Schatten norm. HS_1, HS_F, and HS_∞ denoted Hessian nuclear ($p = 1$), Hessian Frobenius ($p = 2$), and Hessian spectral norms ($p = \infty$), respectively. Fig. 2 shows the convergence curves of reconstruction methods with TV, HS_∞, HS_1, and HS_F, for the CatPhan 600 phantom. Note that the reconstruction method used for TV is the MM method

V. Experimental Results

A. Parameters Setting

CBCT reconstruction always involves a trade-off between image resolution and noise level. Most evaluation criteria used in this work were related to the noise level. To compare the performance of different penalties, we adjusted the parameter τ in Eq. (3) for each phantom by trial and error so that the reconstruction results had the same noise level in each comparison group [40].

To determine the value of α in Eq.(9), we calculated the value of $\left\|A^T\Sigma^{-1}A\right\|$ for each tested phantom and found that setting α to be 2×10^{10} was enough to assure that $\alpha I - A^T\Sigma^{-1}A$ is positive definite for all phantoms in our experiment.

In all iterative reconstruction algorithms, the attenuation coefficient u was initialized using the FDK reconstruction u_0.

B. Convergence Analysis

The range of the values of objective functions using different penalties can differ significantly, even when using exactly the same regularization parameter τ. To make these objective functions "comparable" in the same plot, we used a normalized objective cost to indicate the convergence of the reconstruction algorithms. The normalized objective cost was defined as the ratio of the objective function value of the reconstruction at the kth iteration and that of the initial reconstruction (using FDK), *i.e.* $\Phi(u_k)/\Phi(u_0)$.

To distinguish between different HS penalty terms, we referred to them as HSp, with p denoting the order of the Schatten norm. HS_1, HS_F, and HS_∞ denoted Hessian nuclear ($p = 1$), Hessian Frobenius ($p = 2$), and Hessian spectral norms ($p = \infty$), respectively. Fig. 2 shows the convergence curves of reconstruction methods with TV, HS_∞, HS_1, and HS_F, for the CatPhan 600 phantom. Note that the reconstruction method used for TV is the MM method

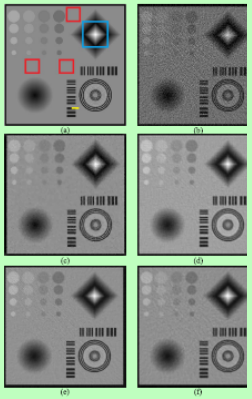

Fig. 3. A representative slice of (a) the original CS phantom; and re
structed images from different reconstructed algorithms with inci
photon number 1×10^5 (low-dose protocol): (b) FDK; (c) TV; (d) H
(e) HS_1; (f) HS_F.

proposed by Sun *et al.* [29], while the method used
the three HS penalties (HS_∞, HS_1, and HS_F) was the
developed in this study. For all penalties, good converge
was achieved after 30 iterations. Fig. 2 shows that all pena
had a similar or close convergence speed.

Note that there was a sub-optimization problem (the
objective function (21). Please see also step 3 in Fig. 1) in
reconstruction process. This dual objective function is sm
and differentiable over Ω. To solve this sub-optimization p
lem, we selected the Nesterov algorithm [47], rather than
classical gradient projection method. Our experiments sho
that, for this sub-optimization problem, the Nesterov algori
can converge in about 20 iterations, while the classical grad
decent method needs at least 80 iterations to converge. Th
consistent with the convergence analysis in the literature [43].

C. CS Phantom

To demonstrate the superiority of our approach over the
TV penalty, we visually compared the reconstructed images
using the proposed HS penalties with those using the TV
penalty for the CS phantom in the low-dose protocol (with
incident photon number 1×10^5). Fig. 3(a) displays a slice

TABLE I
COMPARISONS BETWEEN IMAGES FROM DIFFERENT RECONSTRUCTION ALGORITHMS FOR THE CS

Incident photon	Penalty	Noise level ($\times 10^{-4}$)	PSNR	ISNR	MSSIM	FWHM
1×10^5	FDK	27.00±0.09	18.81±0.09	0.00±0.00	0.12±0.00	N/A
	TV	3.32±0.03	32.63±0.18	8.76±0.01	0.90±0.00	**1.82±0.**
	HS_∞	3.33±0.00	31.94±0.01	8.86±0.00	0.90±0.00	3.75±0.
	HS_1	3.27±0.01	**33.75±0.16**	**9.53±0.01**	**0.93±0.00**	2.22±0.
	HS_F	3.34±0.02	32.14±0.08	8.87±0.01	0.92±0.00	3.69±0.
5×10^5	FDK	12.00±0.00	23.26±0.06	0.00±0.00	0.38±0.00	N/A
	TV	1.68±0.01	36.11±0.06	7.47±0.01	0.95±0.00	**1.43±0.**
	HS_∞	1.78±0.00	37.99±0.02	8.58±0.00	0.98±0.00	2.57±0.
	HS_1	1.76±0.00	**40.12±0.11**	**9.52±0.02**	**0.99±0.00**	2.12±0.
	HS_F	1.77±0.00	37.89±0.11	8.49±0.02	0.98±0.00	3.04±0.

digital CS phantom itself were repeated eight times, and the
evaluation indexes were expressed as mean ± std.

Table I shows that the SIR algorithms using TV and
the HS penalty family all had much better reconstruction
quality than FDK, according to all evaluation indexes. In fact,
the evaluation indexes of the SIR reconstruction algorithms at
the low-dose protocol were better than the FDK at the high-
dose protocol. At the low-dose protocol, the HS_1 penalty gave
the best result, in terms of PSNR, ISNR, and SSIM. The HS_∞
and HS_F penalty had similar reconstruction quality as the TV
penalty, all slightly lower than the HS_1 penalty. At the high-
dose protocol, the HS_1 penalty had the best result in terms
of PSNR, ISNR, and SSIM, with the HS_F penalty following
behind. All three HS penalties produced better reconstruc-
tion quality than the TV penalty, in terms of PSNR, ISNR,
and SSIM.

The TV penalty had the smallest FWHM value, indicating
that it produced the reconstruction image with the sharpest
edges (thus, the highest resolution). The FDK results at
both protocols were too noisy to calculate the FWHM in
Table I. Among the HS penalties, the HS_1 penalty had the
smallest FWHM, indicating a better edge preserving ability.
These numerical observations are consistent with the visual
inspection of Fig. 3, where the HS penalty family tended to
slightly blur image edges, while the TV penalty preserved
edges better.

D. Shepp-Logan phantom

The reconstruction results using different penalties for the
modified Shepp-Logan phantom also showed that the proposed
HS penalties can avoid the staircase effect (Fig. 5). The blue
rectangle in Fig. 5(a) denotes the ROI, which is magnified and
displayed in the lower-right corner of Fig. 5(a); corresponding
ROIs are magnified and displayed in the lower-right corners
of Figs. 5(b-f). The FDK result looks very noisy, especially
in the ROI (Fig. 5(b)), and the reconstructed result using the
TV penalty shows an obvious staircase effect in the magnified
region (Fig. 5(c)). The ROIs reconstructed by the HS penalties
(Figs. 5(d-f)) had higher visual quality than those reconstructed
by either FDK or TV.

The intensity curves along the yellow line in Fig. 5(a)
show that the TV-based reconstruction (Fig. 6(c)) had several
staircase artifacts, but the reconstructed results using the HS
penalties (Figs. 6(d-f)) were much smoother. The profiles

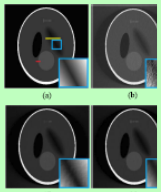

Fig. 5. Representative slices from the
different penalty terms: (a) Original image
(e) HS_1; (f) HS_F.

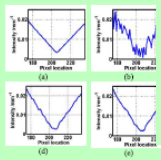

Fig. 6. Profiles through the ellipsoid object (the yellow line in Fig. 5(a)):
(a) Original image; (b) FDK; (c) TV; (d) HS_∞; (e) HS_1; and (f) HS_F.

indicating greater similarity [29], [49]. As the window moved
pixel-by-pixel over the reconstructed image and the reference
image, we obtained an SSIM map. In practice, we used a
single Mean-SSIM (MSSIM) value to evaluate the overall
image quality by averaging the SSIM values over a pre-defined
region. In Table I, we used original CS image as the reference
image to calculate the SSIM. For both the low-dose and high-
dose protocols, all reconstructions and the simulation of the

TABLE II
CNRs OF DIFFERENT ROIs OF THE CATPHAN 600 PHANTOM

	Noise($\times10^{-4}$)	ROI1	ROI2	ROI3	ROI4
FDK_10mA	35	0.29	0.37	0.45	0.64
FDK_80mA	13	0.58	0.83	0.94	1.03
TV	7.60	0.61	1.16	1.21	1.27
HS_∞	8.25	0.66	1.17	1.14	1.34
HS_1	7.86	0.68	**1.29**	**1.26**	**1.42**
HS_F	7.87	**0.69**	1.27	1.20	1.40

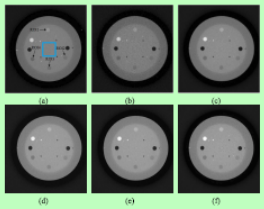

Fig. 7. Representative slices from the reconstructed CatPhan
600 images. (a) FDK with a high-dose protocol (60mA/10ms); Low-dose
protocol (10mA/10ms): (b) FDK, (c) TV, (d) HS_∞, (e) HS_1, (f) HS_F.

FWHM value, indicating that the TV penalty produced the
reconstructed image with the sharpest edges, and the HS
penalties produced reconstructed images with edges that were
less sharp.

E. CatPhan 600 Phantom

The reconstructed CatPhan 600 images show that the low-
dose protocol (10mA/10ms) results using TV (Fig. 7(c)),
HS_∞ (Fig. 7(d)), HS_1 (Fig. 7(e)), and HS_F (Fig. 7(f)) penal-
ties had significantly better visual quality than the low-dose
protocol FDK result (Fig. 7(b)). To quantitatively compare
the penalties' abilities to suppress noise, the blue rectangle
in Fig. 7(a) was chosen to calculate the noise level. The black
arrows indicate the regions selected to calculate CNR values.

Table II lists CNRs of the four ROIs from different algo-
rithms. The high-dose FDK result had a higher CNR value
than the low-dose FDK result. The TV and HS reconstructions
had higher CNR values than the high-dose and low-dose FDK
results. The HS penalties and the TV penalty had comparable
CNR values, indicating that the HS penalties and the TV
penalty can comparably suppress noise in the reconstructed
images. The HS_1 penalty ($p = 1$) had a slightly higher CNR
values than the other two HS penalties in most cases.

F. Anthropomorphic Head Phantom

Fig. 8 displays the reconstructed anthropomorphic head
phantom images. The black rectangle in Fig. 8(a) denotes the

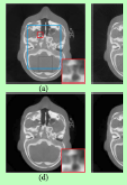

Fig. 8. Representative slices o
head phantom image using diffe
tocol (80mA/10ms); Low-dose pr
(d) HS_∞; (e) HS_1; and (f) HS_F.

TA
MSSIM OF THE BLUE

Penalty	Noise le
FDK_10mA	
FDK_80mA	8
TV	7
HS_∞	7
HS_1	7
HS_F	7

ROI selected to calculate th
represents the region we sel
the reconstructed image and
high-dose FDK result as the
penalties could produce com
in Fig. 8(a) is magnified a
corner of Fig. 8(a); corresp
displayed in the lower-righ
the TV result (Fig. 8(c)) has
the HS penalty family result
but slightly blurred.

MSSIM values calculated
the reference image in the
We also show the SSIM maps in Fig. 9. The value of each
pixel in the SSIM map measures the structural similarity
between the targeted image and the reference image in the
11×11 window regions centered on each voxel.

The MSSIM values in the blue ROI corresponding to the
low-dose FDK, TV, HS_∞, HS_1, and HS_F are 0.74, 0.79,
0.86, 0.93, and 0.92, respectively (Table III). The three HS
penalties had higher MSSIM values than the TV penalty,
indicating that the HS penalties were better able to preserve
local structures than TV. According to the MSSIM values,
the HS_1 penalty had the best reconstruction result, while the
HS_F penalty followed rather closely. The differences between
different penalties' ability to preserve local structures are better
demonstrated in Fig. 9, where the SSIM map resulting from the

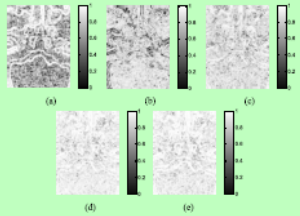

Fig. 9. SSIM maps from the low dose reconstructed image over
the reference image (FDK reconstructed image using the high dose
protocol): (a) FDK (MSSIM = 0.74); (b) TV (MSSIM = 0.79); (c) HS_∞
(MSSIM = 0.86); (d) HS_1 (MSSIM = 0.93); (e) HS_F (MSSIM = 0.92).

displayed in Fig. 6 confirmed the HS penalties' ability to
avoid the staircase effect. To quantitatively analyze the penalty
terms' performance in preserving edges during CBCT recon-
struction, we studied the FWHM of the reconstructed images
along the red line in Fig. 5(a). Different penalties exhibited
clear differences in sharpness along the red line. The FWHM
corresponding to TV, HS_∞, HS_1, and HS_F was 2.03, 3.14,
3.48, and 3.49, respectively. The TV penalty has the smallest
HS_1 penalty looks the whitest, indicating the best performance
in preserving local structures over the selected ROI. The
HS_F penalty showed the second best ability to preserve local
structures.

VI. Discussion

The penalty term in SIR reflects the prior information
of the underlying image. Different penalty terms can be
constructed based on different prior information. The TV
penalty has demonstrated its superiority in preserving edges
in image processing and CBCT reconstruction. However,
the TV penalty can sometimes lead to the staircase effect. Our
experiments demonstrated the staircase effect in the CS phan-
tom (Figs. 3-4(c)), the Shepp-Logan phantom (Figs. 5-6(c)),
and the anthropomorphic head phantom (Fig. 8(c)). The over-
sharpening of regions that are not piecewise constant may wipe
out some important details in the underlying image, leading
to a false interpretation. To overcome the staircase effect and
improve the quality of the reconstructed image, we proposed
in this study to use the HS penalty family, instead of the TV
penalty, for CBCT reconstruction. Our experiments showed
that the HS penalty family performed well in avoiding the
staircase effect and preserving image regions with smooth
intensity transitions (Figs. 3-6(e, f, g) and Fig. 8(e, f, g)). The
MSSIM values and the SSIM maps for the anthropomorphic
head phantom also demonstrated this (Fig. 9).

Among the HS penalties tested, the HS_1 penalty yielded
the best reconstruction results in most cases, closely followed
by the HS_F penalty. The improvement due to the HS_∞
penalty is less pronounced, perhaps because the HS_∞ penalty
considers only the maximum absolute eigenvalue that satisfies
the threshold criteria. In other words, the HS_∞ penalty failed
to include additional information that other eigenvalues might
have provided.

The FWHM comparison in the Shepp-Logan phantom indi-
cated that the HS penalty family does not preserve edges as
well as the TV penalty. This seems to be a common limitation
for the second-order penalties that has been observed in a
previous study of the Hessian penalty [29]. Shi *et al.* [30]
combined TV and Hessian penalties using a local structure
adaptive strategy for CBCT reconstruction, where the asso-
ciated objective function was not convex anymore and an
alternative minimization method was used for the optimization
process. A similar strategy can be used in the future to
combine the HS penalty family with the TV penalty for 3D
CBCT reconstruction to preserve both sharp edges and regions
with smooth intensity transitions. However, the optimization
method should be re-designed.

In this study, the performance of different penalties for
CBCT reconstruction was evaluated under the same noise level
by adjusting the regularization parameter [40]. Different strate-
gies can be potentially used for the performance evaluation.
For example, Han *et al.* [20] evaluated the constrained TV
minimization-based reconstruction with parameters selected to
have the highest performance according to different utility
metrics characterizing either reconstruction contrast or spatial
resolution. Thus the selected optimal parameters are strongly
metric-dependent [20]. In this work, we tuned the parameters
for different algorithms such that the reconstructed images
were at the same noise level and then compared algorithm
performance at the matched noise level [40]. Therefore,
the parameters we used for TV reconstruction may not be
optimal according to different metrics defined in [20]. We will
compare the proposed penalties with TV by choosing metric-
specific optimal parameters in a future work similar to that
in [20]. As the parameters were not adjusted to be optimal
according to certain specific evaluation metrics in our experi-
ments, undesired artifacts existed in the reconstructed images
in some cases. For example, the HS_1 slice (CS phantom) in
Fig. 4(d) has localized diagonal stripe high-frequency artifacts
at its lower middle portion. These artifacts can be removed
using a larger regularization parameter with a stronger noise
suppressing ability but a lower spatial resolution. For the four
small dots in Fig. 7, the HS_∞ (Fig. 7(d)) and HS_1 (Fig. 7(e))
penalties tended to reconstruct them to faint line segments.
This could be related to the anisotropic spatial resolution
property of the used penalties. Similar trend was also observed
in the image reconstructed by the TV penalty (Fig. 7(c)).
These dots can be better restored by reconstructing images
with a higher resolution through adjusting the regularization
parameter.

VII. Conclusion

In this study, we proposed to use the HS penalty family
for 3D CBCT reconstruction, and we developed an effec-
tive algorithm to minimize the objective function using the
majorization-minimization approach followed by a primal-dual
formulation. Both simulated and physical experiments showed
that the HS penalty family can effectively reconstruct the
underlying three-dimensional image and preserve regions with
smooth intensity transitions without introducing the staircase
effect often induced by the TV penalty. Among the three HS
penalties ($p = 1$, $p = 2$, and $p = \infty$), the one with $p = 1$
performed the best in most cases, followed by the HS penalty
with $p = 2$. However, since it consists of the second-order
derivatives, the HS penalty family tends to slightly blur sharp
edges in the reconstruction results. A possible remedy is to

讨论

- 论文重要部分，对所进行的研究、实验、观察到的材料进行归纳、概括和探讨
- 探讨实验观察的结果是否与有关假设相符，说明预期外的事实
- 与自己过去的或者其它作者的结果及其理论解释比较、分析异同及可能的原因，提出自己的见解、评价其意义。
- 根据理论分析、仿真或实验结果讨论不同参数产生的变化，理论分析与实验相符的程度以及可能出现的问题等
- 同类研究的国内、外研究动态及与本文的关系。
- 研究过程中遇到的问题、误差和教训。尚待解决的问题及可能的解决方法。对发现的异常暂无资料支持或未能解释者，讨论中也应提及，留待今后研究解决。
- 实验结果的理论根据及其应用价值。指出实验结果的理论意义及对实践的指导作用
- 作用机制或变化规律的探讨。可引用他人或其他领域的研究成果以说明和支持自己的观点和结果。
- 今后的研究方向、改进方法的设想和建议。
- 不要回避实验本身的缺点及与已有理论相反的结果。
- …

1. 引经据典，分析异同，解释矛盾…
2. 除了主要结论为，不要太武断，多用“would，maybe, might, possibly…”

结论(Conclusions)

又称总结。

- 与前言提出的问题遥相呼应，对整个研究成果做出总判断、总评价(Quick summary)。
- 研究结果说明了什么问题，得到了什么规律，揭示了什么原理，解决了什么理论或者实际问题，有何新的见解，以及有哪些不足之处和尚待解决的问题等 (Future work)。

重要的事情说三次：摘要、前言和结论

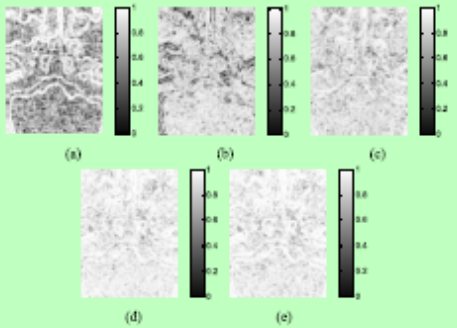

Fig. 9. SSIM maps from the low dose reconstructed image over the reference image (FDK reconstructed image using the high dose protocol): (a) FDK (MSSIM = 0.74); (b) TV (MSSIM = 0.79); (c) HS_∞ (MSSIM = 0.86); (d) HS_1 (MSSIM = 0.93); (e) HS_F (MSSIM = 0.92).

HS_1 penalty looks the whitest, indicating the best performance in preserving local structures over the selected ROI. The HS_F penalty showed the second best ability to preserve local structures.

VI. Discussion

The penalty term in SIR reflects the prior information of the underlying image. Different penalty terms can be constructed based on different prior information. The TV penalty has demonstrated its superiority in preserving edges in image processing and CBCT reconstruction. However, the TV penalty can sometimes lead to the staircase effect. Our experiments demonstrated the staircase effect in the CS phantom (Figs. 3-4(c)), the Shepp-Logan phantom (Figs. 5-6(c)), and the anthropomorphic head phantom (Fig. 8(c)). The over-sharpening of regions that are not piecewise constant may wipe out some important details in the underlying image, leading to a false interpretation. To overcome the staircase effect and improve the quality of the reconstructed image, we proposed in this study to use the HS penalty family, instead of the TV penalty, for CBCT reconstruction. Our experiments showed that the HS penalty family performed well in avoiding the staircase effect and preserving image regions with smooth intensity transitions (Figs. 3-6(e, f, g) and Fig. 8(e, f, g)). The MSSIM values and the SSIM maps for the anthropomorphic head phantom also demonstrated this (Fig. 9).

Among the HS penalties tested, the HS_1 penalty yielded the best reconstruction results in most cases, closely followed by the HS_F penalty. The improvement due to the HS_∞ penalty is less pronounced, perhaps because the HS_∞ penalty considers only the maximum absolute eigenvalue that satisfies the threshold criteria. In other words, the HS_∞ penalty failed to include additional information that other eigenvalues might have provided.

The FWHM comparison in the Shepp-Logan phantom indicated that the HS penalty family does not preserve edges as well as the TV penalty. This seems to be a common limitation for the second-order penalties that has been observed in a previous study of the Hessian penalty [29]. Shi *et al.* [30] combined TV and Hessian penalties using a local structure adaptive strategy for CBCT reconstruction, where the associated objective function was not convex anymore and an alternative minimization method was used for the optimization process. A similar strategy can be used in the future to combine the HS penalty family with the TV penalty for 3D CBCT reconstruction to preserve both sharp edges and regions with smooth intensity transitions. However, the optimization method should be re-designed.

In this study, the performance of different penalties for CBCT reconstruction was evaluated under the same noise level by adjusting the regularization parameter [40]. Different strategies can be potentially used for the performance evaluation. For example, Han *et al.* [20] evaluated the constrained TV minimization-based reconstruction with parameters selected to have the highest performance according to different utility metrics charactering either reconstruction contrast or spatial resolution. Thus the selected optimal parameters are strongly metric-dependent [20]. In this work, we tuned the parameters for different algorithms such that the reconstructed images were at the same noise level and then compared algorithm performance at the matched noise level [40]. Therefore, the parameters we used for TV reconstruction may not be optimal according to different metrics defined in [20]. We will compare the proposed penalties with TV by choosing metric-specific optimal parameters in a future work similar to that in [20]. As the parameters were not adjusted to be optimal according to certain specific evaluation metrics in our experiments, undesired artifacts existed in the reconstructed images in some cases. For example, the HS_1 slice (CS phantom) in Fig. 4(d) has localized diagonal stripe high-frequency artifacts at its lower middle portion. These artifacts can be removed using a larger regularization parameter with a stronger noise suppressing ability but a lower spatial resolution. For the four small dots in Fig. 7, the HS_∞ (Fig. 7(d)) and HS_1 (Fig. 7(e)) penalties tended to reconstruct them to faint line segments. This could be related to the anisotropic spatial resolution property of the used penalties. Similar trend was also observed in the image reconstructed by the TV penalty (Fig. 7(c)). These dots can be better restored by reconstructing images with a higher resolution through adjusting the regularization parameter.

VII. Conclusion

In this study, we proposed to use the HS penalty family for 3D CBCT reconstruction, and we developed an effective algorithm to minimize the objective function using the majorization-minimization approach followed by a primal-dual formulation. Both simulated and physical experiments showed that the HS penalty family can effectively reconstruct the underlying three-dimensional image and preserve regions with smooth intensity transitions without introducing the staircase effect often induced by the TV penalty. Among the three HS penalties ($p = 1$, $p = 2$, and $p = \infty$), the one with $p = 1$ performed the best in most cases, followed by the HS penalty with $p = 2$. However, since it consists of the second-order derivatives, the HS penalty family tends to slightly blur sharp edges in the reconstruction results. A possible remedy is to

致谢(Acknowledgements)

- 对给予本文研究的选题、构思、实验或撰写等方面给予指导、帮助或建议的人员致以谢意；
- 资助单位致谢。

致谢

非正常致谢：

最学术的求婚

ELSEVIER

Physica A

journal homepage: www.elsevier.com/locate/physa

Performance analysis for minimally nonlinear irreversible refrigerators at finite cooling power

Rui Long *, Zhichun Liu, Wei Liu *

School of Energy and Power Engineering, Huazhong University of Science and Technology, 1037 Luoyu Road, Wuhan 430074, China

HIGHLIGHTS

- The minimally nonlinear model is adopted to analyze the performance of refrigerators .
- COP and its bounds at given cooling power for different operating regions are deduced.
- COP bounds under the χ figure of merit at finite cooling power are calculated.
- Relative gain in COP in different operating regions is presented.

ARTICLE INFO

Article history:
Received 7 July 2017
Received in revised form 29 October 2017
Available online 1 January 2018

Keywords:
Minimally nonlinear irreversible refrigerators
Coefficient of performance
Finite cooling power

ABSTRACT

The coefficient of performance (COP) for general refrigerators at finite cooling power have been systematically researched through the minimally nonlinear irreversible model, and its lower and upper bounds in different operating regions have been proposed. Under the tight coupling conditions, we have calculated the universal COP bounds under the χ figure of merit in different operating regions. When the refrigerator operates in the region with lower external flux, we obtained the general bounds ($0 < \varepsilon < (\sqrt{9+8\varepsilon_C}-3)/2$) under the χ figure of merit. We have also calculated the universal bounds for maximum gain in COP under different operating regions to give a further insight into the COP gain with the cooling power away from the maximum one. When the refrigerator operates in the region located between maximum cooling power and maximum COP with lower external flux, the upper bound for COP and the lower bound for relative gain in COP present large values, compared to a relative small loss from the maximum cooling power. If the cooling power is the main objective, it is desirable to operate the refrigerator at a slightly lower cooling power than at the maximum one, where a small loss in the cooling power induces a much larger COP enhancement.

Acknowledgments

We acknowledge the support received from the National Natural Science Foundation of China (51706076, 51736004). In addition, Rui Long wants to thank, in particular, the patience, care and support from Panpan Mao over the passed years. Will you marry me?

References

[1] S. Carnot, Reflexions sur la Puissance Motorice Du Feu Et sur Les Machines, Ecole Polytechnique, Paris, 1824.
[2] V. Holubec, A. Ryabov, Work and power fluctuations in a critical heat engine, 2017, arXiv preprint arXiv:170502371.
[3] M. Polettini, M. Esposito, Carnot efficiency at divergent power output, 2016, arXiv preprint arXiv:161108192.
[4] J.S. Lee, H. Park, Carnot efficiency is attainable in an irreversible process, 2016, arXiv preprint arXiv:161107665.
[5] M. Campisi, R. Fazio, The power of a critical heat engine, Nat. Commun. 7 (2016) 11895.
[6] C.V. Johnson, Approaching the Carnot limit at finite power: An exact solution, 2017, arXiv preprint arXiv:170306119.
[7] V. Holubec, A. Ryabov, Diverging, but negligible power at Carnot efficiency: theory and experiment, 2017, arXiv preprint arXiv:170806261.
[8] F.L. Curzon, B. Ahlborn, Efficiency of a Carnot engine at maximum power output, Amer. J. Phys. 43 (1) (1975) 22.
[9] R. Long, W. Liu, Coefficient of performance and its bounds for general refrigerators with nonisothermal processes, J. Phys. A 47 (32) (2014) 325002.
[10] R. Long, W. Liu, Unified trade-off optimization for general heat devices with nonisothermal processes, Phys. Rev. E 91 (4) (2015) 042127.

致谢

非正常致谢：

最后，要感谢我的女朋友，在我22年的生命中始终没有出现过，让我得以专心于学术，顺利完成本科论文。

2021年最感人致谢

“理想不伟大，只愿年过半百，归来仍是少年，希望还有机会重新认识这个世界，不辜负这一生吃过的苦。最后如果还能做出点让别人生活更美好的事，那这辈子就赚了。”

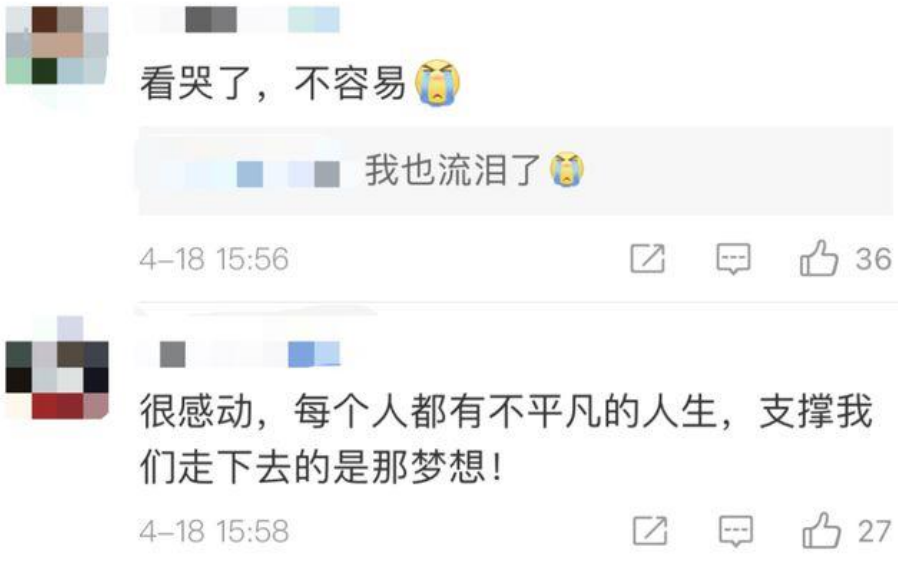

致谢

我走了很远的路，吃了很多的苦，才将这份博士学位论文送到你的面前。二十二载求学路，一路风雨泥泞，许多不容易。如梦一场，仿佛昨天一家人才团聚过。

出生在一个小山坳里，母亲在我十二岁时离家。父亲在家的日子不多，即便在我病得不能自己去医院的时候，也仅是留下勉强够治病的钱后又走了。我十七岁时，他因交通事故离世后，我哭得稀里糊涂，因为再得重病时没有谁来管我了。同年，和我住在一起的婆婆病故，真的无能为力。她照顾我十七年，下葬时却仅是一副薄薄的棺材。另一个家庭成员是老狗小花，为父亲和婆婆守过坟，后因我进城上高中而命不知何时何处所终。如兄长般的计算机启蒙老师邱浩没能看到我的大学录取通知书，对我照顾有加的师母也在不惑之前匆匆离开人世。每次回去看他们，这一座座坟茔都提示着生命的每一分钟都弥足珍贵。

人情冷暖，生离死别，固然让人痛苦与无奈，而贫穷则可能让人失去希望。家徒四壁，在煤油灯下写作业或者读书都是晚上最开心的事。如果下雨，保留节目就是用竹笋壳塞瓦缝防漏雨。高中之前的主要经济来源是夜里抓黄鳝、周末钓鱼、养小猪崽和出租水牛。那些年里，方圆十公里的水田和小河都被我用脚测量过无数次。被狗和蛇追，半夜落水，因蓄电瓶进水而摸黑逃回家中；学费没交，黄鳝却被父亲偷卖了，然后买了肉和酒，都是难以避免的事。

人后的苦尚且还能克服，人前的尊严却无比脆弱。上课的时候，因拖欠学费而经常被老师叫出教室约谈。雨天湿漉着上课，屁股后面说不定还是泥。夏天光着脚走在滚烫的路上。冬天穿着破旧衣服打着寒颤穿过那条长长的过道领作业本。这些都可能成为压垮骆驼的最后一根稻草。如果不是考试后常能从主席台领奖金，顺便能贴一墙奖状满足最后的虚荣心，我可能早已放弃。

身处命运的漩涡，耗尽心力去争取那些可能本就是稀松平常的东西，每次转折都显得那么的身不由己。幸运的是，命运到底还有一丝怜惜。进入高中后，学校免了全部学杂费，胡叔叔一家帮助解决了生活费。进入大学后，计算机终于成了我一生的事业与希望，胃溃疡和胃出血也终与我作别。

从家出发坐大巴需要两个半小时才能到县城，一直盼着走出大山。从炬光乡小学、大寅镇中学、仪陇县中学、绵阳市南山中学，到重庆的西南大学，再到中科院自动化所，我也记不清有多少次因为现实的压力而觉得自己快扛不下去了。这一路，信念很简单，把书念下去，然后走出去，不枉活一世。世事难料，未来注定还会面对更为复杂的局面。但因为有了这些点点滴滴，我已经有勇气和耐心面对任何困难和挑战。理想不伟大，只愿年过半百，归来仍是少年，希望还有机会重新认识这个世界，不辜负这一生吃过的苦。最后如果还能做出点让别人生活更美好的事，那这辈子就赚了。

致谢

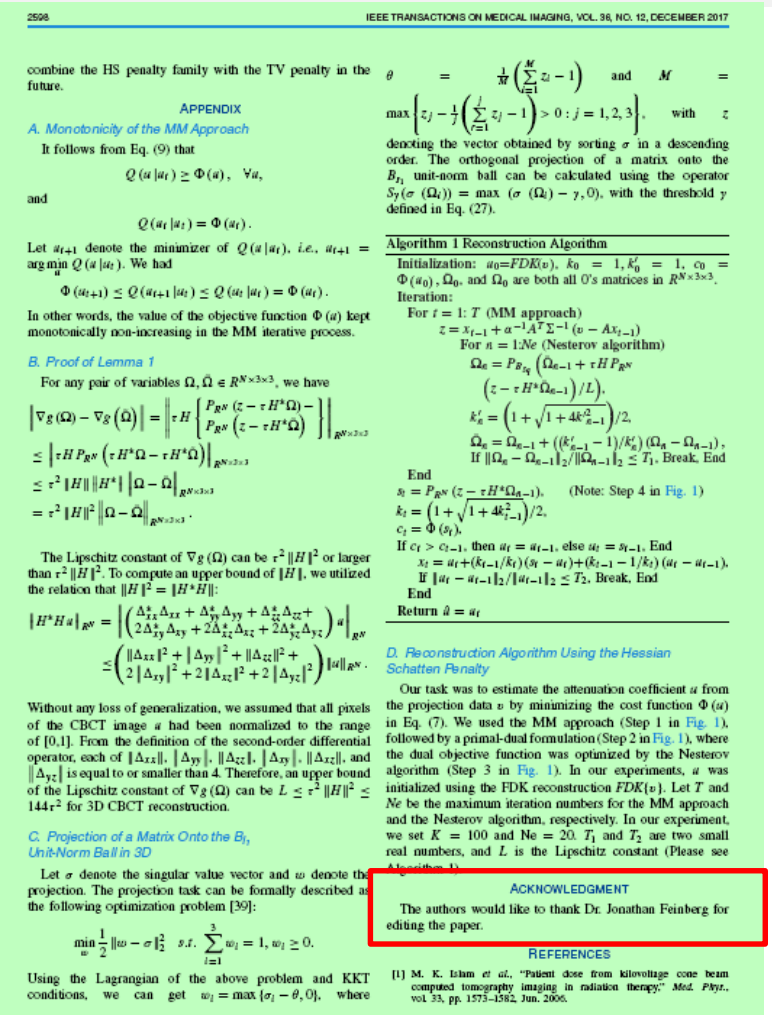

2598 IEEE TRANSACTIONS ON MEDICAL IMAGING, VOL. 36, NO. 12, DECEMBER 2017

combine the HS penalty family with the TV penalty in the future.

APPENDIX

A. Monotonicity of the MM Approach

It follows from Eq. (9) that

$$Q(u|u_t) \geq \Phi(u), \quad \forall u,$$

and

$$Q(u_t|u_t) = \Phi(u_t).$$

Let u_{t+1} denote the minimizer of $Q(u|u_t)$, *i.e.*, $u_{t+1} = \arg\min_u Q(u|u_t)$. We had

$$\Phi(u_{t+1}) \leq Q(u_{t+1}|u_t) \leq Q(u_t|u_t) = \Phi(u_t).$$

In other words, the value of the objective function $\Phi(u)$ kept monotonically non-increasing in the MM iterative process.

B. Proof of Lemma 1

For any pair of variables $\Omega, \hat{\Omega} \in R^{N\times3\times3}$, we have

$$\begin{aligned}\left|\nabla g(\Omega) - \nabla g(\hat{\Omega})\right| &= \left|\tau H \left\{ \begin{matrix} P_{R^N}(z - \tau H^*\Omega) - \\ P_{R^N}(z - \tau H^*\hat{\Omega}) \end{matrix} \right\}\right|_{R^{N\times3\times3}} \\ &\leq \left|\tau H P_{R^N}(\tau H^*\Omega - \tau H^*\hat{\Omega})\right|_{R^{N\times3\times3}} \\ &\leq \tau^2 \|H\| \|H^*\| \left|\Omega - \hat{\Omega}\right|_{R^{N\times3\times3}} \\ &= \tau^2 \|H\|^2 \left\|\Omega - \hat{\Omega}\right\|_{R^{N\times3\times3}}.\end{aligned}$$

The Lipschitz constant of $\nabla g(\Omega)$ can be $\tau^2\|H\|^2$ or larger than $\tau^2\|H\|^2$. To compute an upper bound of $\|H\|$, we utilized the relation that $\|H\|^2 = \|H^*H\|$:

$$\begin{aligned}\left|H^*Hu\right|_{R^N} &= \left|\begin{pmatrix} \Delta_{xx}^*\Delta_{xx} + \Delta_{yy}^*\Delta_{yy} + \Delta_{zz}^*\Delta_{zz} + \\ 2\Delta_{xy}^*\Delta_{xy} + 2\Delta_{xz}^*\Delta_{xz} + 2\Delta_{yz}^*\Delta_{yz} \end{pmatrix} u\right|_{R^N} \\ &\leq \left(\begin{matrix} \|\Delta_{xx}\|^2 + \left|\Delta_{yy}\right|^2 + \|\Delta_{zz}\|^2 + \\ 2\left|\Delta_{xy}\right|^2 + 2\left|\Delta_{xz}\right|^2 + 2\left|\Delta_{yz}\right|^2 \end{matrix}\right)\|u\|_{R^N}.\end{aligned}$$

Without any loss of generalization, we assumed that all pixels of the CBCT image u had been normalized to the range of [0,1]. From the definition of the second-order differential operator, each of $\|\Delta_{xx}\|$, $\left|\Delta_{yy}\right|$, $\|\Delta_{zz}\|$, $\left|\Delta_{xy}\right|$, $\|\Delta_{xz}\|$, and $\left|\Delta_{yz}\right|$ is equal to or smaller than 4. Therefore, an upper bound of the Lipschitz constant of $\nabla g(\Omega)$ can be $L \leq \tau^2\|H\|^2 \leq 144\tau^2$ for 3D CBCT reconstruction.

C. Projection of a Matrix Onto the B_{l_1} Unit-Norm Ball in 3D

Let σ denote the singular value vector and w denote the projection. The projection task can be formally described as the following optimization problem [39]:

$$\min_w \frac{1}{2}\|w - \sigma\|_2^2 \quad s.t. \sum_{i=1}^{3} w_i = 1, w_i \geq 0.$$

Using the Lagrangian of the above problem and KKT conditions, we can get $w_i = \max\{\sigma_i - \theta, 0\}$, where $\theta = \frac{1}{M}\left(\sum_{i=1}^{M} z_i - 1\right)$ and $M = \max\left\{z_j - \frac{1}{j}\left(\sum_{r=1}^{j} z_j - 1\right) > 0 : j = 1, 2, 3\right\}$, with z denoting the vector obtained by sorting σ in a descending order. The orthogonal projection of a matrix onto the B_{l_1} unit-norm ball can be calculated using the operator $S_\gamma(\sigma(\Omega_i)) = \max(\sigma(\Omega_i) - \gamma, 0)$, with the threshold γ defined in Eq. (27).

Algorithm 1 Reconstruction Algorithm

Initialization: u_0=*FDK*(v), $k_0 = 1, k_0' = 1, c_0 = \Phi(u_0)$, Ω_0, and Ω_0 are both all 0's matrices in $R^{N\times3\times3}$.
Iteration:
For $t = 1$: T (MM approach)
$z = x_{t-1} + \alpha^{-1}A^T\Sigma^{-1}(v - Ax_{t-1})$
For $n = 1$:Ne (Nesterov algorithm)
$\Omega_n = P_{B_{l_1}}\left(\hat{\Omega}_{n-1} + \tau H P_{R^N}\left(z - \tau H^*\hat{\Omega}_{n-1}\right)/L\right)$,
$k_n' = \left(1 + \sqrt{1 + 4k_{n-1}'^2}\right)/2$,
$\hat{\Omega}_n = \Omega_{n-1} + \left((k_{n-1}' - 1)/k_n'\right)(\Omega_n - \Omega_{n-1})$,
If $\|\Omega_n - \Omega_{n-1}\|_2/\|\Omega_{n-1}\|_2 \leq T_1$, Break, End
End
$s_t = P_{R^N}(z - \tau H^*\Omega_{n-1})$, (Note: Step 4 in Fig. 1)
$k_t = \left(1 + \sqrt{1 + 4k_{t-1}^2}\right)/2$,
$c_t = \Phi(s_t)$,
If $c_t > c_{t-1}$, then $u_t = u_{t-1}$, else $u_t = s_{t-1}$, End
$x_t = u_t + (k_{t-1}/k_t)(s_t - u_t) + (k_{t-1} - 1/k_t)(u_t - u_{t-1})$,
If $\|u_t - u_{t-1}\|_2/\|u_{t-1}\|_2 \leq T_2$, Break, End
End
Return $\hat{u} = u_t$

D. Reconstruction Algorithm Using the Hessian Schatten Penalty

Our task was to estimate the attenuation coefficient u from the projection data v by minimizing the cost function $\Phi(u)$ in Eq. (7). We used the MM approach (Step 1 in Fig. 1), followed by a primal-dual formulation (Step 2 in Fig. 1), where the dual objective function was optimized by the Nesterov algorithm (Step 3 in Fig. 1). In our experiments, u was initialized using the FDK reconstruction *FDK*(v). Let T and Ne be the maximum iteration numbers for the MM approach and the Nesterov algorithm, respectively. In our experiment, we set $K = 100$ and Ne = 20. T_1 and T_2 are two small real numbers, and L is the Lipschitz constant (Please see Algorithm 1).

ACKNOWLEDGMENT

The authors would like to thank Dr. Jonathan Feinberg for editing the paper.

REFERENCES

[1] M. K. Islam *et al.*, "Patient dose from kilovoltage cone beam computed tomography imaging in radiation therapy," *Med. Phys.*, vol. 33, pp. 1573–1582, Jun. 2006.

ACKNOWLEDGMENT

The authors would like to thank Dr. Jonathan Feinberg for editing the paper.

致谢

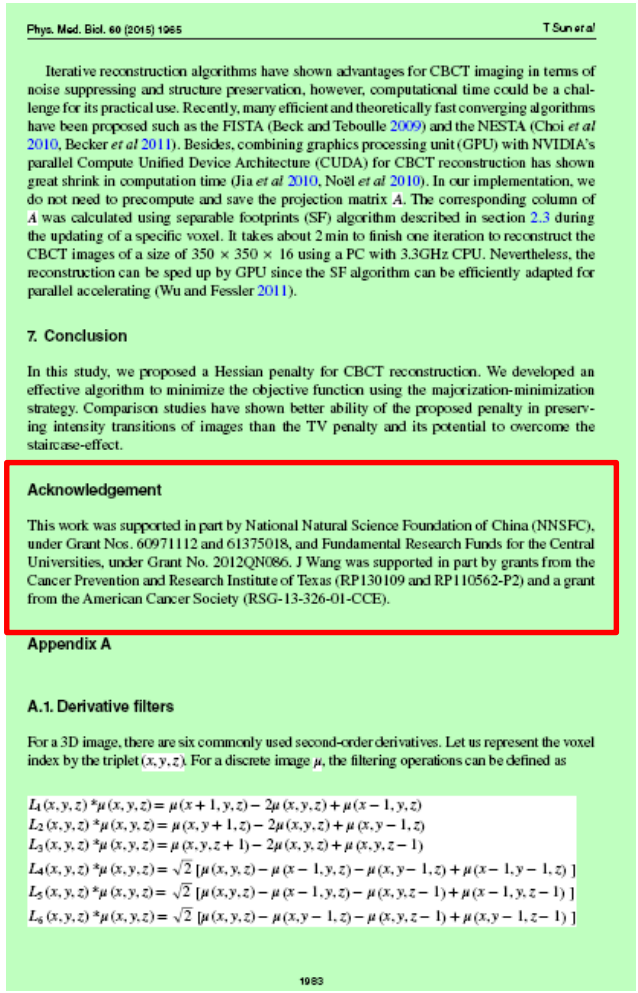

Phys. Med. Biol. 60 (2015) 1965 T Sun et al

Iterative reconstruction algorithms have shown advantages for CBCT imaging in terms of noise suppressing and structure preservation, however, computational time could be a challenge for its practical use. Recently, many efficient and theoretically fast converging algorithms have been proposed such as the FISTA (Beck and Teboulle 2009) and the NESTA (Choi *et al* 2010, Becker *et al* 2011). Besides, combining graphics processing unit (GPU) with NVIDIA's parallel Compute Unified Device Architecture (CUDA) for CBCT reconstruction has shown great shrink in computation time (Jia *et al* 2010, Noël *et al* 2010). In our implementation, we do not need to precompute and save the projection matrix A. The corresponding column of A was calculated using separable footprints (SF) algorithm described in section 2.3 during the updating of a specific voxel. It takes about 2 min to finish one iteration to reconstruct the CBCT images of a size of 350 × 350 × 16 using a PC with 3.3GHz CPU. Nevertheless, the reconstruction can be sped up by GPU since the SF algorithm can be efficiently adapted for parallel accelerating (Wu and Fessler 2011).

7. Conclusion

In this study, we proposed a Hessian penalty for CBCT reconstruction. We developed an effective algorithm to minimize the objective function using the majorization-minimization strategy. Comparison studies have shown better ability of the proposed penalty in preserving intensity transitions of images than the TV penalty and its potential to overcome the staircase-effect.

Acknowledgement

This work was supported in part by National Natural Science Foundation of China (NNSFC), under Grant Nos. 60971112 and 61375018, and Fundamental Research Funds for the Central Universities, under Grant No. 2012QN086. J Wang was supported in part by grants from the Cancer Prevention and Research Institute of Texas (RP130109 and RP110562-P2) and a grant from the American Cancer Society (RSG-13-326-01-CCE).

Appendix A

A.1. Derivative filters

For a 3D image, there are six commonly used second-order derivatives. Let us represent the voxel index by the triplet (x, y, z). For a discrete image μ, the filtering operations can be defined as

$$
\begin{aligned}
L_1(x,y,z) * \mu(x,y,z) &= \mu(x+1,y,z) - 2\mu(x,y,z) + \mu(x-1,y,z) \\
L_2(x,y,z) * \mu(x,y,z) &= \mu(x,y+1,z) - 2\mu(x,y,z) + \mu(x,y-1,z) \\
L_3(x,y,z) * \mu(x,y,z) &= \mu(x,y,z+1) - 2\mu(x,y,z) + \mu(x,y,z-1) \\
L_4(x,y,z) * \mu(x,y,z) &= \sqrt{2}\,[\mu(x,y,z) - \mu(x-1,y,z) - \mu(x,y-1,z) + \mu(x-1,y-1,z)\,] \\
L_5(x,y,z) * \mu(x,y,z) &= \sqrt{2}\,[\mu(x,y,z) - \mu(x-1,y,z) - \mu(x,y,z-1) + \mu(x-1,y,z-1)\,] \\
L_6(x,y,z) * \mu(x,y,z) &= \sqrt{2}\,[\mu(x,y,z) - \mu(x,y-1,z) - \mu(x,y,z-1) + \mu(x,y-1,z-1)\,]
\end{aligned}
$$

1983

参考文献

- 科学有继承性，现在的研究大都在过去的研究基础上进行的；若使用前人材料，而不引用文献，有抄袭或剽窃嫌疑；
- 正确、可信、及时、全面的参考文献引用（论据），奠定了你的研究基础，有助于读者相信你的观点和论证。(增加可信度的一种方式)

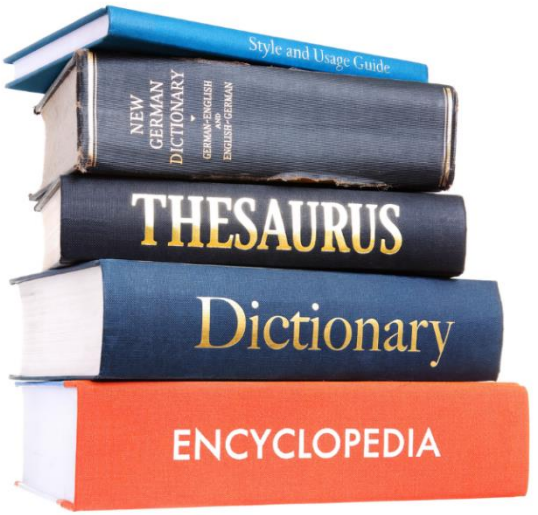

科技论文写作：所言必有出处

参考文献的引用能增加论文的可信度

某些品种的苹果成熟时变红，是因为其中含有较多红色素；红色素的形成与苹果所受的日照长短有关；当日照不足，苹果就不会变红**（证据一）**。我们买到的苹果就有可能不是红色的**（结论）**。我们的实验确实如此。**（证据二）**

读者的反应：我不知道作者的证据一是怎么得到的，我不知道作者是不是在胡说八道。

某些品种的苹果成熟时变红，是因为其中含有较多红色素[1]；红色素的形成与苹果所受的日照长短有关[2]；当日照不足，苹果就不会变红[3]**（证据一）**。我们买到的苹果就有可能不是红色的**（结论）**。我们的实验确实如此。**（证据二）**

读者的反应：作者所列证据有科学根据，他的推理过程也是对的。我觉得作者的结论是正确的。

参考文献

[1] 爱因斯坦，Science, Vol. 600, pp.238, 1940.
[2] 达尔文，Nature, Vol. 500, pp.130, 1850.
[3] 牛顿，Nature, Vol. , pp. 200, 1700.

参考文献

参考文献一般是经过Peer Review的科技文献:

- 商业性报纸、杂志、书籍等的引用要慎之又慎(学术性出版单位的书籍和期刊一般更加可信)
- 自谋体的引用慎之又慎。比如： Trump, D, J. @ realDonaldTrump, 10:00am May 6 2020.
- 引用表示你获取信息的来源，不能有太多级别太低的期刊或者会议。

可列于参考文献表的文献类型包括图书、期刊、会议论文集、专利和学位论文等。

参考文献

采用规范化的著录形式： 统一标准的的书写符号、标注方法和书写次序

中文：

中国国家标准：GB/T 7714-2015《信息与文献 参考文献著录规则》

学位论文参阅学校要求

外文

- **APA (American Psychological Association) style** ：Education, Psychology, and Sciences
- **MLA (Modern Language Association) style** ：Humanities
- **Chicago style** ：Business, History, and the Fine Arts
- **IEEE style**: Engineering

*** 投稿前，你需要了解相关期刊或者会议论文集对引用格式的要求。方法：查阅期刊或者会议的Guide for Authors, 下载期刊或者会议论文的专用模板、Latex style文档、Endnote参考格式文档等。**

附录(Appendix)

- 附录不是文章的必要组成部分，但可为深入了解本文人员提供参考
- 主要提供论文有关公式推导、演算以及不宜列入正文的数据和图表等

一般原则

- 对于插入正文后有损条理性和完整性的材料
- 篇幅太大的材料
- 对一般非专业读者并非重要，但对专业同行有重要参考价值。

combine the HS penalty family with the TV penalty in the future.

APPENDIX

A. Monotonicity of the MM Approach

It follows from Eq. (9) that

$$Q(u|u_t) \geq \Phi(u), \quad \forall u,$$

and

$$Q(u_t|u_t) = \Phi(u_t).$$

Let u_{t+1} denote the minimizer of $Q(u|u_t)$, *i.e.*, $u_{t+1} = \arg\min_u Q(u|u_t)$. We had

$$\Phi(u_{t+1}) \leq Q(u_{t+1}|u_t) \leq Q(u_t|u_t) = \Phi(u_t).$$

In other words, the value of the objective function $\Phi(u)$ kept monotonically non-increasing in the MM iterative process.

B. Proof of Lemma 1

For any pair of variables $\Omega, \bar{\Omega} \in R^{N\times 3\times 3}$, we have

$$\begin{aligned}
\left|\nabla g(\Omega) - \nabla g\left(\bar{\Omega}\right)\right| &= \left\| \tau H \left\{ \begin{matrix} P_{R^N}(z - \tau H^* \Omega) - \\ P_{R^N}\left(z - \tau H^* \bar{\Omega}\right) \end{matrix} \right\} \right|_{R^{N\times 3\times 3}} \\
&\leq \left| \tau H P_{R^N}\left(\tau H^* \Omega - \tau H^* \bar{\Omega}\right) \right|_{R^{N\times 3\times 3}} \\
&\leq \tau^2 \|H\| \|H^*\| \left|\Omega - \bar{\Omega}\right|_{R^{N\times 3\times 3}} \\
&= \tau^2 \|H\|^2 \left\|\Omega - \bar{\Omega}\right\|_{R^{N\times 3\times 3}}.
\end{aligned}$$

The Lipschitz constant of $\nabla g(\Omega)$ can be $\tau^2\|H\|^2$ or larger than $\tau^2\|H\|^2$. To compute an upper bound of $\|H\|$, we utilized the relation that $\|H\|^2 = \|H^*H\|$:

$$\begin{aligned}
\left|H^*Hu\right|_{R^N} &= \left| \begin{pmatrix} \Delta_{xx}^* \Delta_{xx} + \Delta_{yy}^* \Delta_{yy} + \Delta_{zz}^* \Delta_{zz} + \\ 2\Delta_{xy}^* \Delta_{xy} + 2\Delta_{xz}^* \Delta_{xz} + 2\Delta_{yz}^* \Delta_{yz} \end{pmatrix} u \right|_{R^N} \\
&\leq \left(\begin{matrix} \|\Delta_{xx}\|^2 + \left|\Delta_{yy}\right|^2 + \|\Delta_{zz}\|^2 + \\ 2\left|\Delta_{xy}\right|^2 + 2\|\Delta_{xz}\|^2 + 2\left|\Delta_{yz}\right|^2 \end{matrix} \right) \|u\|_{R^N}.
\end{aligned}$$

Without any loss of generalization, we assumed that all pixels of the CBCT image u had been normalized to the range of [0,1]. From the definition of the second-order differential operator, each of $\|\Delta_{xx}\|$, $\left|\Delta_{yy}\right|$, $\|\Delta_{zz}\|$, $\left|\Delta_{xy}\right|$, $\|\Delta_{xz}\|$, and $\left|\Delta_{yz}\right|$ is equal to or smaller than 4. Therefore, an upper bound of the Lipschitz constant of $\nabla g(\Omega)$ can be $L \leq \tau^2\|H\|^2 \leq 144\tau^2$ for 3D CBCT reconstruction.

C. Projection of a Matrix Onto the B_{T_1} Unit-Norm Ball in 3D

Let σ denote the singular value vector and ω denote the projection. The projection task can be formally described as the following optimization problem [39]:

$$\min_{w} \frac{1}{2}\|w - \sigma\|_2^2 \quad s.t. \quad \sum_{i=1}^{3} w_i = 1, w_i \geq 0.$$

Using the Lagrangian of the above problem and KKT conditions, we can get $w_i = \max\{\sigma_i - \theta, 0\}$, where $\theta = \frac{1}{M}\left(\sum_{i=1}^{M} z_i - 1\right)$ and $M = \max\left\{z_j - \frac{1}{j}\left(\sum_{r=1}^{j} z_j - 1\right) > 0 : j = 1, 2, 3\right\}$, with z denoting the vector obtained by sorting σ in a descending order. The orthogonal projection of a matrix onto the B_{T_1} unit-norm ball can be calculated using the operator $S_\gamma(\sigma(\Omega_i)) = \max(\sigma(\Omega_i) - \gamma, 0)$, with the threshold γ defined in Eq. (27).

Algorithm 1 Reconstruction Algorithm

Initialization: $u_0 = FDK(v)$, $k_0 = 1, k_0' = 1$, $c_0 = \Phi(u_0)$, Ω_0, and $\bar{\Omega}_0$ are both all 0's matrices in $R^{N\times 3\times 3}$.
Iteration:
  For $t = 1{:}\,T$ (MM approach)
    $z = x_{t-1} + \alpha^{-1} A^T \Sigma^{-1}(v - Ax_{t-1})$
    For $n = 1{:}Ne$ (Nesterov algorithm)
      $\Omega_n = P_{B_{T_1}}\left(\bar{\Omega}_{n-1} + \tau H P_{R^N}\left(z - \tau H^* \bar{\Omega}_{n-1}\right)/L\right)$,
      $k_n' = \left(1 + \sqrt{1 + 4k_{n-1}'^2}\right)/2$,
      $\bar{\Omega}_n = \Omega_{n-1} + \left((k_{n-1}' - 1)/k_n'\right)(\Omega_n - \Omega_{n-1})$,
      If $\|\Omega_n - \Omega_{n-1}\|_2 / \|\bar{\Omega}_n\|_2 \leq T_1$, Break, End
    End
    $s_t = P_{R^N}(z - \tau H^* \bar{\Omega}_{n-1})$. (Note: Step 4 in Fig. 1)
    $k_t = \left(1 + \sqrt{1 + 4k_{t-1}^2}\right)/2$,
    $c_t = \Phi(s_t)$,
    If $c_t > c_{t-1}$, then $u_t = u_{t-1}$, else $u_t = s_{t-1}$, End
    $x_t = u_t + (k_{t-1}/k_t)(s_t - u_t) + (k_{t-1} - 1/k_t)(u_t - u_{t-1})$,
    If $\|u_t - u_{t-1}\|_2 / \|u_{t-1}\|_2 \leq T_2$, Break, End
  End
Return $\hat{u} = u_t$

D. Reconstruction Algorithm Using the Hessian Schatten Penalty

Our task was to estimate the attenuation coefficient u from the projection data v by minimizing the cost function $\Phi(u)$ in Eq. (7). We used the MM approach (Step 1 in Fig. 1), followed by a primal-dual formulation (Step 2 in Fig. 1), where the dual objective function was optimized by the Nesterov algorithm (Step 3 in Fig. 1). In our experiments, u was initialized using the FDK reconstruction $FDK(v)$. Let T and Ne be the maximum iteration numbers for the MM approach and the Nesterov algorithm, respectively. In our experiment, we set $K = 100$ and $Ne = 20$. T_1 and T_2 are two small real numbers, and L is the Lipschitz constant (Please see Algorithm 1).

ACKNOWLEDGMENT

The authors would like to thank Dr. Jonathan Feinberg for editing the paper.

REFERENCES

[1] M. K. Islam *et al.*, "Patient dose from kilovoltage cone beam computed tomography imaging in radiation therapy," *Med. Phys.*, vol. 33, pp. 1573–1582, Jun. 2006.

Iterative reconstruction algorithms have shown advantages for CBCT imaging in terms of noise suppressing and structure preservation, however, computational time could be a challenge for its practical use. Recently, many efficient and theoretically fast converging algorithms have been proposed such as the FISTA (Beck and Teboulle 2009) and the NESTA (Choi *et al* 2010, Becker *et al* 2011). Besides, combining graphics processing unit (GPU) with NVIDIA's parallel Compute Unified Device Architecture (CUDA) for CBCT reconstruction has shown great shrink in computation time (Jia *et al* 2010, Noël *et al* 2010). In our implementation, we do not need to precompute and save the projection matrix A. The corresponding column of A was calculated using separable footprints (SF) algorithm described in section 2.3 during the updating of a specific voxel. It takes about 2 min to finish one iteration to reconstruct the CBCT images of a size of 350 × 350 × 16 using a PC with 3.3GHz CPU. Nevertheless, the reconstruction can be sped up by GPU since the SF algorithm can be efficiently adapted for parallel accelerating (Wu and Fessler 2011).

7. Conclusion

In this study, we proposed a Hessian penalty for CBCT reconstruction. We developed an effective algorithm to minimize the objective function using the majorization-minimization strategy. Comparison studies have shown better ability of the proposed penalty in preserving intensity transitions of images than the TV penalty and its potential to overcome the staircase-effect.

Acknowledgement

This work was supported in part by National Natural Science Foundation of China (NNSFC), under Grant Nos. 60971112 and 61375018, and Fundamental Research Funds for the Central Universities, under Grant No. 2012QN086. J Wang was supported in part by grants from the Cancer Prevention and Research Institute of Texas (RP130109 and RP110562-P2) and a grant from the American Cancer Society (RSG-13-326-01-CCE).

Appendix A

A.1. Derivative filters

For a 3D image, there are six commonly used second-order derivatives. Let us represent the voxel index by the triplet (x, y, z). For a discrete image μ, the filtering operations can be defined as

$$
\begin{aligned}
&L_1(x,y,z) * \mu(x,y,z) = \mu(x+1,y,z) - 2\mu(x,y,z) + \mu(x-1,y,z)\\
&L_2(x,y,z) * \mu(x,y,z) = \mu(x,y+1,z) - 2\mu(x,y,z) + \mu(x,y-1,z)\\
&L_3(x,y,z) * \mu(x,y,z) = \mu(x,y,z+1) - 2\mu(x,y,z) + \mu(x,y,z-1)\\
&L_4(x,y,z) * \mu(x,y,z) = \sqrt{2}\,[\mu(x,y,z) - \mu(x-1,y,z) - \mu(x,y-1,z) + \mu(x-1,y-1,z)]\\
&L_5(x,y,z) * \mu(x,y,z) = \sqrt{2}\,[\mu(x,y,z) - \mu(x-1,y,z) - \mu(x,y,z-1) + \mu(x-1,y,z-1)]\\
&L_6(x,y,z) * \mu(x,y,z) = \sqrt{2}\,[\mu(x,y,z) - \mu(x,y-1,z) - \mu(x,y,z-1) + \mu(x,y-1,z-1)]
\end{aligned}
$$

A.2. Update of $w_{ji}^{\prime(l)}$

In section 3.3, we introduced the majorization-minimization approach to upper-bound the original penalty function with a quadratic form. The difference of the TV penalty and the proposed Hessian penalty lies in the matrix $R^{(l)}$, where $R^{(l)}$ is $R_{\mathrm{TV}}^{(l)}$ or $R_{\mathrm{Hessian}}^{(l)}$ in equations (18) and (19), specifically. Obviously, $R_{\mathrm{Hessian}}^{(l)}$ has more non-zero elements than $R_{\mathrm{TV}}^{(l)}$ alongside the main diagonal. For voxel μ_j, N_j is the set of neighbor voxels which are at most 2-voxel far from it. With the definition in equation (22), we can easily obtain that $w_{ji}^{\prime(l)} := -R_{ji}^{(l)}/2$, $\mu_i \in N_j$, $i \neq j$. $w_{ji}^{\prime(l)}$ is updated in each iteration. For the TV penalty, the detailed update formula of $w_{ji}^{\prime(l)}$ can be referred in Wang *et al* (2008b). For the proposed Hessian penalty, we first defined $W(x, y, z)$ as

$$W(x,y,z) := \frac{1}{\sqrt{\sum_{i=1}^{6} [L_i(x,y,z) * \mu^{(l)}(x,y,z)]^2}}$$

where L_i is the derivative filter defined in the previous section. The update formula of $w_{ji}^{\prime(l)}$ can be expressed as:

For each neighbor voxel $\mu_i \in N_j$ of voxel μ_j

$$
\begin{aligned}
&\text{if } i=(x+1,y,z) \text{ then } w_{ji}^{\prime(l)} = W(x,y,z) + 3W(x+1,y,z) + W(x+1,y+1,z) + W(x+1,y,z+1)\\
&\text{if } i=(x,y+1,z) \text{ then } w_{ji}^{\prime(l)} = W(x,y,z) + 3W(x,y+1,z) + W(x+1,y+1,z) + W(x,y+1,z+1)\\
&\text{if } i=(x,y,z+1) \text{ then } w_{ji}^{\prime(l)} = W(x,y,z) + 3W(x,y,z+1) + W(x+1,y,z+1) + W(x,y+1,z+1)\\
&\text{if } i=(x-1,y,z) \text{ then } w_{ji}^{\prime(l)} = W(x-1,y,z) + 3W(x,y,z) + W(x,y+1,z) + W(x,y,z+1)\\
&\text{if } i=(x,y-1,z) \text{ then } w_{ji}^{\prime(l)} = W(x,y-1,z) + 3W(x,y,z) + W(x,y,z+1) + W(x+1,y,z)\\
&\text{if } i=(x,y,z-1) \text{ then } w_{ji}^{\prime(l)} = W(x,y,z-1) + 3W(x,y,z) + W(x+1,y,z) + W(x,y+1,z)\\
&\text{if } i=(x,y+1,z+1) \text{ then } w_{ji}^{\prime(l)} = -W(x,y+1,z+1)\\
&\text{if } i=(x,y+1,z-1) \text{ then } w_{ji}^{\prime(l)} = -W(x,y+1,z)\\
&\text{if } i=(x,y-1,z-1) \text{ then } w_{ji}^{\prime(l)} = -W(x,y,z)\\
&\text{if } i=(x,y-1,z+1) \text{ then } w_{ji}^{\prime(l)} = -W(x,y,z+1)\\
&\text{if } i=(x+1,y,z+1) \text{ then } w_{ji}^{\prime(l)} = -W(x+1,y,z+1)\\
&\text{if } i=(x+1,y,z-1) \text{ then } w_{ji}^{\prime(l)} = -W(x+1,y,z)\\
&\text{if } i=(x-1,y,z-1) \text{ then } w_{ji}^{\prime(l)} = -W(x,y,z)\\
&\text{if } i=(x-1,y,z+1) \text{ then } w_{ji}^{\prime(l)} = -W(x,y,z+1)\\
&\text{if } i=(x+1,y+1,z) \text{ then } w_{ji}^{\prime(l)} = -W(x+1,y+1,z)\\
&\text{if } i=(x+1,y-1,z) \text{ then } w_{ji}^{\prime(l)} = -W(x+1,y,z)\\
&\text{if } i=(x-1,y-1,z) \text{ then } w_{ji}^{\prime(l)} = -W(x,y,z)\\
&\text{if } i=(x-1,y+1,z) \text{ then } w_{ji}^{\prime(l)} = -W(x,y+1,z)\\
&\text{if } i=(x+2,y,z) \text{ then } w_{ji}^{\prime(l)} = -W(x+1,y,z)/2\\
&\text{if } i=(x,y+2,z) \text{ then } w_{ji}^{\prime(l)} = -W(x,y+1,z)/2\\
&\text{if } i=(x,y,z+2) \text{ then } w_{ji}^{\prime(l)} = -W(x,y,z+1)/2\\
&\text{if } i=(x-2,y,z) \text{ then } w_{ji}^{\prime(l)} = -W(x-1,y,z)/2\\
&\text{if } i=(x,y-2,z) \text{ then } w_{ji}^{\prime(l)} = -W(x,y-1,z)/2\\
&\text{if } i=(x,y,z-2) \text{ then } w_{ji}^{\prime(l)} = -W(x,y,z-1)/2
\end{aligned}
$$

A.3. Gauss–Seidel update

The task for image reconstruction is to estimate the attenuation coefficient distribution map μ from the projection data $\bar{p}$ by minimizing equation (3). In this study, the Gauss-Seidel update algorithm was adopted for the minimization problem.

Initialization:

$$\mu = \mathrm{FDK}\{\bar{p}\}$$

$$r = \bar{p} - A\mu$$

$$s_j = A_j{}^T \Sigma^{-1} A_j, \ \forall j$$

For each iteration
Begin
For each pixel μ_j
Begin

$$\mathrm{update}\left\{w_{ji}^{(t)}\right\}$$

$$\mu_j^{\mathrm{old}} := \mu_j$$

$$\mu_j^{\mathrm{new}} := \frac{A_j{}^T \Sigma^{-1} r + s_j \mu_j^{\mathrm{old}} + \beta \sum_{i \in N_j} w_{ji}^{(t)} \mu_i}{s_j + \beta \sum_{i \in N_j} w_{ji}^{(t)}}$$

$$\mu_j := \max\left\{\mu_j^{\mathrm{new}}, 0\right\}$$

$$r := r + A_j\left(\mu_j^{\mathrm{old}} - \mu_j\right)$$

End
End

References

Arigovindan M *et al* 2013 High-resolution restoration of 3D structures from widefield images with extreme low signal-to-noise-ratio *Proc. Natl Acad. Sci. USA* **110** 17344–9

Beck A and Teboulle M 2009 A fast iterative shrinkage-thresholding algorithm for linear inverse problems *SIAM J. Imag. Sci.* **2** 183–202

Becker S, Bobin J and Candès E J 2011 NESTA: a fast and accurate first-order method for sparse recovery *SIAM J. Imag. Sci.* **4** 1–39

Boyd S P and Vandenberghe L 2004 *Convex Optimization* (Cambridge: Cambridge University Press)

Brenner D J and Hall E J 2007 Computed tomography: an increasing source of radiation exposure *New Engl. J. Med.* **357** 2277–84

Buades A, Coll B and Morel J-M 2005 A non-local algorithm for image denoising *IEEE Computer Society Conf. on Computer Vision and Pattern Recognition (San Diego, CA, USA, 20–26 June 2005)* pp 60–5

Chan T, Marquina A and Mulet P 2000 High-order total variation-based image restoration *SIAM J. Sci. Comput.* **22** 503–16

Chlewicki W, Hermansen F and Hansen S 2004 Noise reduction and convergence of Bayesian algorithms with blobs based on the Huber function and median root prior *Phys. Med. Biol.* **49** 4717

常用写作软件

写作编辑方式一：所见即所得，手动排版（生物、医学类使用较多）；自动完成参考文献管理

写作编辑方式二：自动排版，强烈建议初学者使用(数学、物理、工学类使用较多)；自动完成参考文献管理

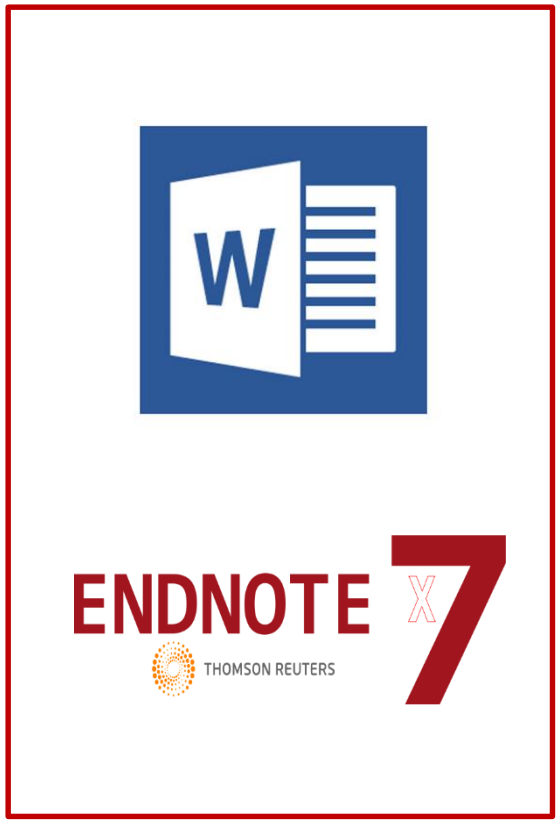

MathType

LaTeX

EndNote

参考文献输入

- 手动为文章添加几十甚至上百篇参考文献，极其繁杂
- 修改过程增删参考文献，需重新编号
- 更改文献格式，可能需重来一遍
- …

总之：费时，费力，易出错

EndNote

- 主要功能：

收集及保存文献　查询及管理文献数据　论文及参考文献撰写

- 文中引用格式(In-text Citation)和文末参考文献格式更新。

数据导入

1. 学术搜索引擎(Google Scholar，Semantic Scholar)
2. 各种数据库：

Web of Science 数据库

http://www.webofknowledge.com/wos

ACM Digital Library

http://dl.acm.org/

IEEE/IEE Electronic Library

http://ieeexplore.ieee.org/Xplore/home.jsp

万方数据库

http://g.wanfangdata.com.cn/

知网数据库

https://www.cnki.net/

……

例. Google Scholar

- ✓ Step 1: [学术搜索设置] →[文献管理软件] → Select [EndNote];
- ✓ Step 2: Search documents
- ✓ Step 3: [导入EndNote]
- ✓ Step 4: Save scholar.enw
- ✓ Step 5: Import to EndNote

- 学术搜索引擎提供的参考文献条目不一定准确，写作后务必仔细检查文末参考文献列表
- 通过Google Scholar 或 Semantic Scholar链接去出版社文章页面，下载参考文献条目，内容更准确、更丰富

问题？

时间：请Email联系

我的名字：谭山

Email：shantan@hust.edu.cn